Journal of Materials Chemistry A

Lithium Oxidation and Electrolyte Decomposition at Li-Metal/Liquid Electrolyte Interfaces

Journal:	*Journal of Materials Chemistry A*
Manuscript ID	TA-ART-05-2020-005132.R1
Article Type:	Paper
Date Submitted by the Author:	27-Jul-2020
Complete List of Authors:	Ospina Acevedo, Francisco; Texas A&M University College Station, Chemical Engineering Guo, Ningxuan; Texas A&M University College Station, Chemical Engineering Balbuena, Perla; Texas AandM University, Chemical Engineering

Lithium Oxidation and Electrolyte Decomposition at Li-Metal/Liquid Electrolyte Interfaces

Francisco Ospina-Acevedo, Ningxuan Guo, and Perla B. Balbuena*

Department of Chemical Engineering, Texas A&M University, College Station, TX 77843

*e-mail: balbuena@tamu.edu

Abstract

We examine the evolution of events occurring when a Li metal surface is in contact with a 2M solution of a Li salt in a solvent or mixture of solvents, via classical molecular dynamics simulations with a reactive force field allowing bond breaking and bond forming. The main events include Li oxidation and electrolyte reduction along with expansion of the Li surface layers forming a porous phase that is the basis for the formation of the solid-electrolyte interphase (SEI) components. Nucleation of the main SEI components (LiF, Li oxides, and some organics) are characterized. The analysis clearly reveals the details of these physical-chemical events as a function of time, during 20 nanoseconds. The effects of the chemistry of the electrolyte on Li oxidation and dissolution in the liquid electrolyte, and SEI nucleation and structure are identified by testing two salts: $LiPF_6$ and $LiCF_3SO_3$, and various solvents including ethers and carbonates and mixtures of them. The kinetics and thermodynamics of Li_6F, the core nuclei in the LiF crystal, is studied by analysis of the MD trajectories, and via density functional theory calculations respectively. The SEI formed in this computational experiment is the "native" film that would form upon contact of the Li foil with the liquid electrolyte. As such, this work is the first in a series of computational experiments that will help elucidating the intricate interphase layer formed during battery cycling using metal anodes.

1. Introduction

Global concerns about the use of fossil fuels as primary energy sources have triggered the production of green energy from renewable sources such as wind or solar energy and the development of energy storage technologies.[1-2] For energy storage purposes, lithium-ion batteries (LIBs) have become among the most important portable storage systems in recent decades,[3-4] portraying an essential part as portable energy sources in popular mobile electronic devices and many other applications. Nonetheless, the battery performance regarding its life cycle, energy density, and stability is far from satisfying the increasing requirements of most complex electronic devices and hybrid/electric cars.[5-8] This points out to the need of advances in battery

technologies.[9] In particular, the lithium−sulfur (Li−S) battery has emerged as one of the most promising options for substituting LIBs, especially for high-performance uses as in electric vehicles, since Li-S batteries bring a theoretical energy density up to five times higher than LIBs, as well as low-toxicity and lower costs.[10-13] However, several limitations have prevented their commercialization, despite almost half a century of research.[14] Regarding the cathode, usually an electronically conductive material such as carbon must be combined with sulfur to overcome its insulating nature.[15-16] Another issue is the formation of long chain polysulfides at the cathode during discharge reactions. These polysulfides are soluble in most liquid electrolytes and can migrate to the anode and be reduced on the lithium-metal surface, further dropping the battery performance.[16-17]

The Li-metal anode is considered an essential component for obtaining the expected Li-S battery performance.[18-19] This is because of Li's extremely low negative electrochemical potential, very high theoretical specific capacity, and low density.[20-21] However, the Li-metal anode has additional issues. Safety concerns arise because of the possibility of cell damage or manufacturing failures due to Li-metal's high reactivity, as well as due to the dendrite formation throughout cycling processes which can cause short circuits if dendrites reach the cathode.[22-24] The electrolyte (salt and solvent) plays a vital role for rapid lithium transport and providing stability even near the highly reactive lithium surface. At the Li surface, electrolyte decomposition due to reduction reactions triggered by their low electrochemical stability leads to the growth of a multicomponent passivating film. This film, known as the solid electrolyte interphase (SEI) may have beneficial passivation properties, [20, 25-35] or, quite the opposite, may be a cause of irreversible capacity loss.[17, 36] The specific film behavior depends on its chemical composition, structure, and thickness. Moreover, it has been found the SEI properties depend largely on the solvent, salt, and additives used as well as on the electrode structure.[17, 37-41]. Therefore, understanding the role of the electrolyte in SEI formation and its properties should be a useful strategy for controlling dendrite formation, reducing the effects of anode degradation and stabilizing the surface, thus, potentially improving the performance, cycling and safety of the batteries.[25, 28, 42-44]

Even though the SEI film is supposed to act as an insulator being a barrier for electron transfer, at the initial nucleation stages its structure may favor electron transport. This may occur because of the differences between the amorphous character of nucleating crystals and their bulk theoretical structures, as has been found in some bulk insulator materials where changes in the electronic conductivity were observed in ultra-thin films showing a semiconductor behavior.[45-48] This capability of conducting electrons of imperfectly formed SEI nuclei and phases could

contribute to the growth mechanism that keeps the SEI forming until it reaches hundreds of nanometers.[49] Another important reason for the continuous SEI growth is the presence of radical charged species that result from the SEI reactions and are able to diffuse toward the vicinity of the electrolyte inducing further reactions.[50] Several experimental and theoretical works have studied the various stages of the SEI formation and growth process[31-32, 40-41, 51-57] while other authors have proposed the formation of artificial SEI layers by pretreating the anode before the battery is assembled.[58-59] For the early stages of the SEI formation it is crucial to improve the understanding of electrolyte decomposition by characterizing the reaction mechanisms of electrolytes typically used in battery systems.[42, 60-62] It is known that carbonate solvents have low stability when implemented with Li-metal anodes, while ether-based solvents like dimethoxyethane (DME) and dioxalane (DOL) have shown better stability with respect to the Li-metal anode and are frequently used for these battery systems.[20, 63] However, solvent and salt molecules decomposition are still observed and in spite of the advances reached both from experimental and theoretical studies, the mechanisms of these processes are not yet well understood.[64]

In this work, we carry out classical reactive molecular dynamics (MD) simulations for studying the initial formation of SEI films occurring by Li oxidation and simultaneous decomposition of electrolyte (salt and solvent) molecules in the liquid phase in contact with the Li-metal electrode. We use lithium hexafluorophosphate ($LiPF_6$) as a salt because its reductive decomposition has been pointed as critical on the SEI formation[65] and lithium trifluoromethanesulfonate (lithium triflate or LiTF) that has shown interesting performance in various systems.[66-68] We study the behavior of the various system components (i.e. Li-metal anode slab, and salt and solvent molecules) when the electrolyte solution is put in contact with the Li metal surface. We follow the evolution of various events including the lithium metal expansion/dissolution, salt and solvent decomposition, and initial nucleation of the SEI intermediates and products as well as the electron exchange among the species. We aim to identify the effects of electrolyte composition on the Li-metal anode behavior and the SEI formation and growth at open circuit conditions. We focus only on the initial stages of SEI formation, concentrated in a specific part of the battery system, and do not examine the Li deposition events occurring when an ionic flux arrives at the anode during charge, and the effects of an applied field. To gain further understanding of the structures and mechanisms of the initial stages of SEI formation, density functional theory (DFT) calculations on initial Li-F were used to evaluate SEI fragments observed in MD simulations. Once optimized structures of such fragments are obtained, we investigated the fragment clustering processes

found at initial stages of SEI nucleation. These simulations provide preliminary estimations for the energies of formation and clustering of LiF fragments.

Our conclusions are focused on the formation of a “native SEI” spontaneously occurring due to the extreme Li reactivity. We expect that the highlights in the formation and growth of the initial SEI layer can help to understand the further mechanisms involved in SEI formation and growth during battery cycling.

2. Computational and system details

Classical reactive MD simulations were carried out using the open source LAMMPS[69] software, and the reactive force field (ReaxFF) developed for the atoms C/H/O/S/Li/F/N relations, where the main interactions were trained for lithium battery materials.[70-71] The main reason to work with ReaxFF is its ability to break and form bonds that is essential for the problem we are investigating.[72] ReaxFF uses the interatomic distances and the partial energy to calculate the bond order, taking into account penalty, lone pair, valence, and torsion energy contributions as they are updated every simulation step. The Morse potential is used to calculate the Van der Waals energy, while the charges for every atom are updated through the charge equilibration method[73-78] using Coulomb interactions.[72] The charge equilibration procedure is important as it approximates the partial charge on every atom by minimizing the electrostatic energy of the system, bringing solution to a large sparse linear system of equations.[77] Successful results have been shown in relation to SEI formation in silicon anodes.[79] The Li crystal was previously optimized with a lattice parameter of 3.443 Å, in good agreement with the theoretical value of 3.44 Å.[80] The Li(100) slab dimensions are 20.66 Å x 20.66 Å x 28.55 Å and the overall cell height is 49.55 Å. Dimethoxyethane (DME), dioxalane (DOL), fluoroethylene carbonate (FEC), and ethylene carbonate (EC) were used as solvents in 2M solutions of lithium hexafluorophosphate ($LiPF_6$) and lithium trifluoromethanesulfonate (lithium triflate or LiTF) salt, respectively. DME, DOL, and EC were used as pure solvents, and DOL and FEC were used as a mixture DOL/FEC 4:1 molar rate. Table 1 summarizes the composition of each system evaluated.

To avoid undesired interactions between the electrolyte molecules and the bottom layers of the slab due to the periodic boundary conditions, the *fix wall*[81] command was implemented in both the bottom and top parts of the slab. The main simulations were carried out in the NVT canonical ensemble at constant number of molecules N, volume V, and temperature T. The temperature was kept constant at 300K using the default Nosé−Hoover thermostat[82] with a time step of 0.2 fs.

Table 1. Composition of each system evaluated during this work. All systems consist of a mixture of salt and organic solvent (s) at 2M concentration of salt.

System	Salt	Solvent	Concentration
1	$LiPF_6$	DME	2 M
2		DOL	2 M
3		DOL+FEC	2 M DOL:FEC = 4:1 molar
4		EC	2 M
5	LiTF	DME	2 M
6		DOL	2 M
7		DOL+FEC	2 M DOL:FEC = 4:1 molar
8		EC	2 M

DFT calculations are performed using Gaussian16[83] and visualized by GaussView[84]. The Boese-Martin for Kinetics (BMK)[85] functional was selected as the hybrid exchange-correlation functional with cc-pvtz[86] triple-zeta basis set. The primary reason for the selection of the BMK functional was used is because we would like our simulation methods to be consistent with prior works of our group.[87] For these systems, we have found that BMK converges easier when comparing with the B3LYP functional. To represent the effect of ethylene carbonate (EC) solvent, an implicit solvent model was implemented by the solvation model based on density (SMD)[88] variation of the integral equation formalism variant of the polarizable continuum model (IEFPCM) method, which is recommended to calculate changes in Gibbs free energy for solvation. Tetrahydrofuran is used as the model solvent in this method with its dielectric constant manually changed to 89.8 to represent EC. Geometric optimizations and frequency calculations are done on all fragments and clusters to obtain optimal geometry and energies. An overall charge of -1 or zero is assigned to each fragment to represent the effect of the additions of lithium ions to negative fragments or the addition of neutral lithium atoms to a neutral fragment. Consequently, all clusters are assigned with either -2, -1, or zero charge corresponding to the addition of two negative fragments, one neutral and one negative fragment, and two neutral fragments. These cases are based on observations in MD simulations.

We first model the Li-F fragment by sequential addition of Li atoms or ions to a fluorine anion. Each time a new Li atom or ion is added to the system, geometric optimizations and frequency calculations are performed. Since the system is small, keeping track of actual charges will lead to unnecessary computational difficulties. Therefore, no matter how many positive lithium ions are

added to the system, the overall charge of the system will always be either neutral or -1. Extra calculations are performed to confirm that a positively charged fragment has approximately the same geometry as the neutral fragment. And higher charges (-2, +2…) cause strong deformation that are unrealistic and not observed in MD simulations. Once optimal geometry for fragments of different sizes are obtained, we place two fragments near each other and perform geometric optimization to investigate possible clustering processes. The free energy of forming clusters are also calculated based on statistical mechanics using properties obtained in frequency calculations as implemented in Gaussian16.

3. Results and Discussion

One of the main points of interest when discussing the Li anode behavior is understanding the nature of Li-slab expansion after the Li metal gets in contact with the liquid electrolyte. We use the word expansion to signify the decrease in the density of the Li metal that starts on the surface layers and is a consequence of the oxidation/dissolution process. We study the evolution of the Li metal density and charge distribution analysis based on the MD trajectories. Figure 1a shows the slab discretization used to analyze the Li-slab expansion through the calculation of the Li-density in each block, and the initial atomic charge distribution is shown in Figure 1b. Figure 1c shows the final configuration reached by System 1 (Table 1) as a result of the reactive interactions at the Li-metal anode/liquid electrolyte interface after an interaction time of 20 ns. Also, the atomic charge distribution (Figure 1d) brings information about the nature of each region after the Li slab has expanded due to Li oxidation and electrolyte reduction. For each salt, four systems were built according to the information in Table 1 and the results are discussed in the following sections.

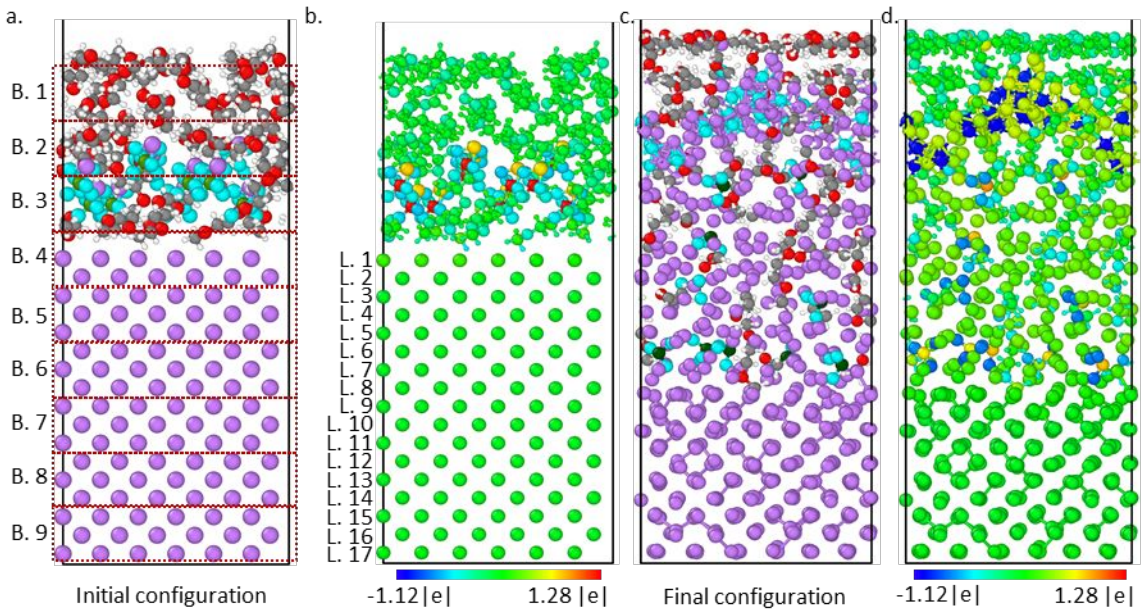

Figure 1. (a) Initial configuration of the simulated system 1 based on $LiPF_6$ electrolyte in a 2M solution of DME, and the block discretization used for Li density analysis, (b) initial electronic charge distribution and layer-labeled slab, and (c, d) final configuration obtained after 20 ns and its charge distribution. Color code for a, c: Li: purple, F: light blue, P: green, O: red, C: grey, H: white. Color code for charge distributions is shown at the bottom of b and d.

3.1 Systems 1 to 4: Electrolyte based on $LiPF_6$ solutions

3.1.1. Li-slab expansion

Because of Li oxidation and dissolution in contact with the electrolyte, Li atomic migration is observed to occur from the Li slab into the electrolyte direction, which decreases the Li atomic density by expanding the slab in the vertical direction (see the contrast of the Li metal atoms position in Fig.1a compared to Fig.1c). To further elucidate these density changes, Figure 2 summarizes the Li-density evolution for each one of the blocks defined in Figure 1a. Figures 2a-d show that in the four $LiPF_6$-based systems in Table 1, the blocks at the bottom (i.e. blocks 7, 8, and 9) keep the bulk Li metal density of ~0.53 g/cc. This behavior implies that the bottom layers remain as a dense phase. For the fourth, fifth and sixth blocks the main expansion varies according to the proximity to the electrolyte. In the case of block 5 (the first block full of Li atoms from the top of the slab), the expansion is almost instantaneous since the beginning of the simulations, while the expansion of block 6 takes longer depending of the extent of the reactions taking place among the anions and some solvent molecules and the partially oxidized Li atoms already in the low density region, being less drastic for the less reactive component (DOL, Figure 2b) and faster and more drastic for the EC-based system (Figure 2d). The density in the top of

the cell (blocks 1 to 3) depends on how the electrolyte allows the partially oxidized Li atoms to reach higher positions, but an average of ~0.2 g/cc is in agreement with the high porosity evidenced from the top region of

Figure 3a and b. Note that the very top region (block 1, light blue line in Figure 2), has an even lower Li density, usually lower than 0.1 g/cc. This is usually Li ions still reaching higher positions and reacting with solvent molecules at the top of the cell.

Figure 2. Li-density evolution for Li slab blocks (refer to Figure 1a for block discretization) from $LiPF_6$-based systems 1 to 4: (a) DME, (b) DOL, (c) mix of DOL and FEC, and (d) EC. Color code:

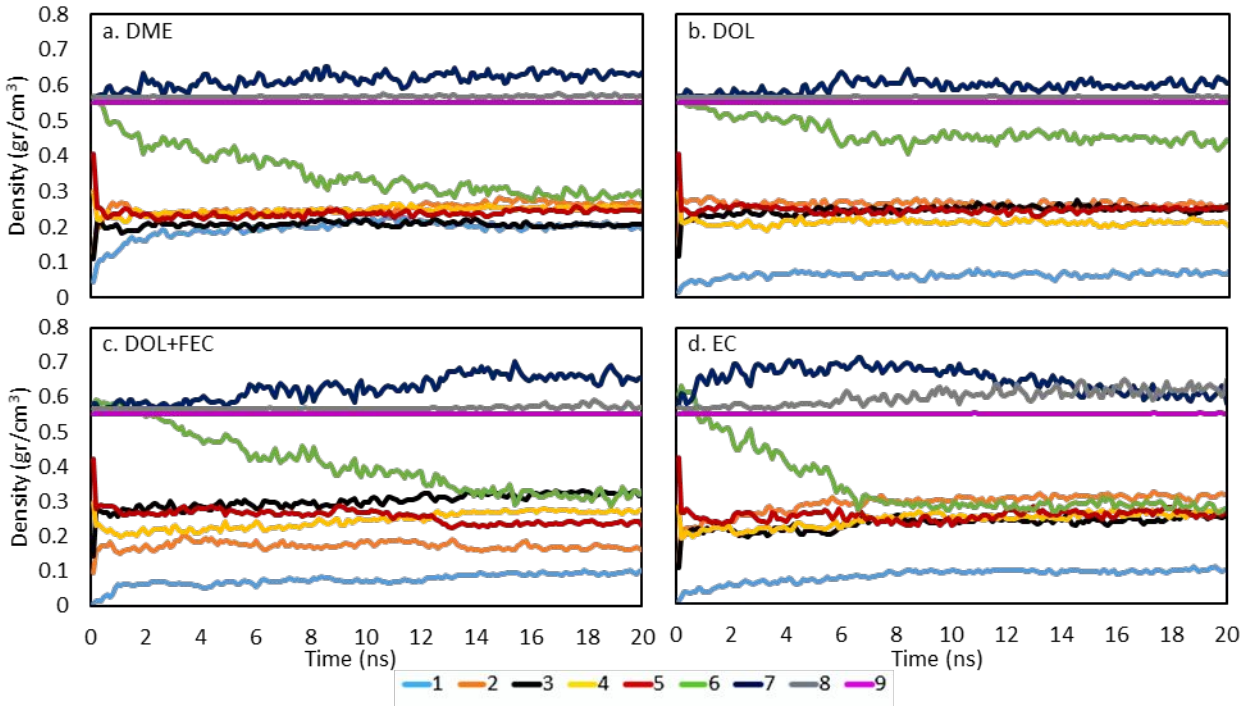

light blue for top block 1, orange for block 2, black for block 3, yellow for block 4, red for block 5, green for block 6, dark blue for block 7, grey for block 8, and purple for bottom block 9.

Figure S1 shows the density evolution of the blocks considering all the species present. In all four systems, the low density in the upper blocks is due to the accumulation of no reacting solvent molecules and the initial formation of the SEI layer close to the upper section of the porous phase as discussed in later sections.

3.1.2. Li charge evolution

As mentioned above, one of the reasons why this expansion of the Li phase occurs, is the existence of interactive redox reactions among the Li-slab atoms and the electrolyte phase. As a result, there is a change in the oxidation state of the Li-atoms and in other components.

Figure 3a and b show the behavior of the Li-slab atoms and their charge distribution after expansion.

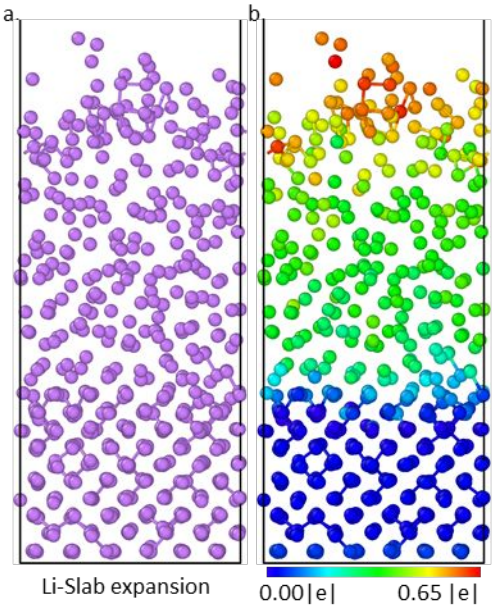

Figure 3. Li-metal slab after 20 ns of simulation. (a) Li slab expands along with the dissolution of Li atoms into the electrolyte and contrasting phases can be recognized due to the different reactions that take place. (b) Charge evolution for the Li-slab atoms, where one can recognize that the bottom layers keep the slab structure almost unaltered and neutral while the expanded atoms reach distinct oxidation levels according to the interaction in the different regions. Color code for charge distributions is shown at the bottom of b.

On the other hand, Figure 4 summarizes the charge evolution per Li-atom averaged in each one of the ten top layers of the slab (the layers are numbered from 1 to 17 from top to bottom as shown in Figure 1b). As observed from Figure 2, from the total 17 Li-layers that compose the Li-slab, the bottom seven (blocks 1 and 2) keep their bulk structure and density (dense phase); block 7 experiences a small density increase in some of the systems but quickly goes back to normal density, while the top eight layers (blocks 4 to 6) expand (defining a porous phase) and become active in the reactions that take place in all four systems evaluated. Following this behavior, the charge evolution of all atoms in each layer was tracked. Figure 4a and b are comparable and show relatively progressive charge variation from the top layer to the internal 10^{th} layer.

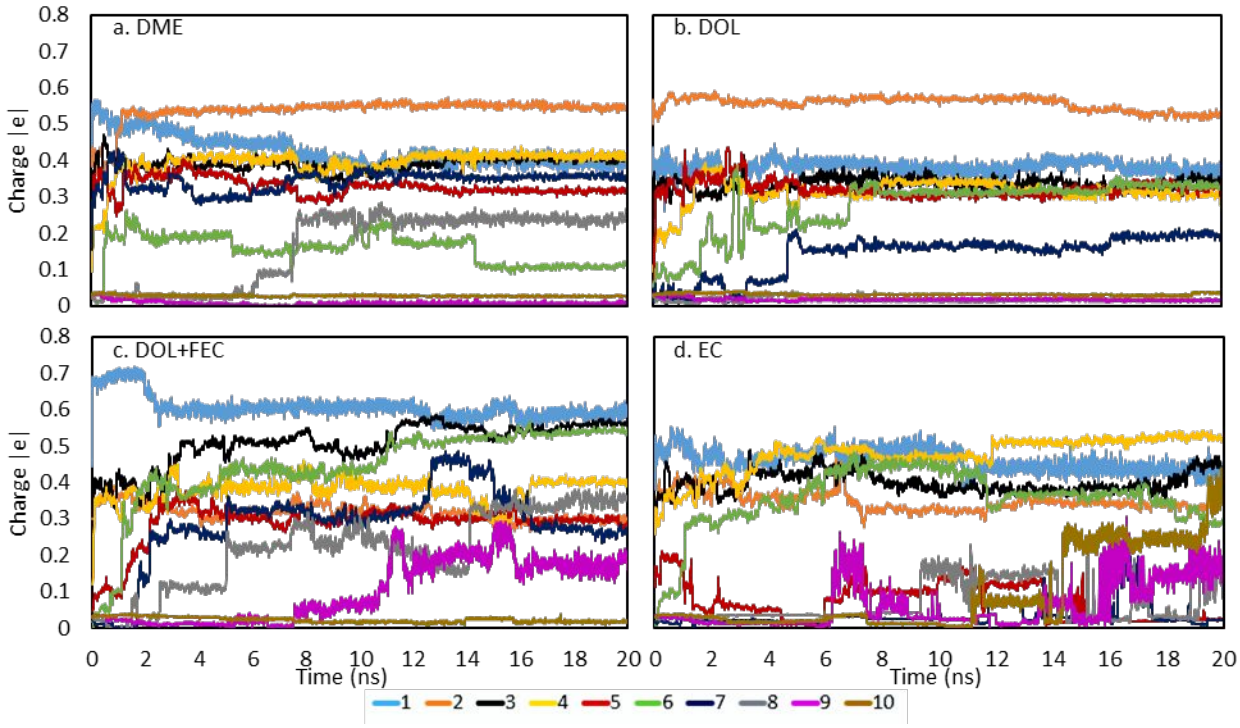

Figure 4. Charge evolution for Li-slab top layers 1 to 10 (refer to Figure 1b. for Li-slab layers numbering) for $LiPF_6$ in various solvents: (a) DME, (b) DOL, (c) mix of DOL and FEC, and (d) EC. Color code: light blue for top layer 1, orange for layer 2, black for layer 3, yellow for layer 4, red for layer 5, green for layer 6, dark blue for layer 7, grey for layer 8, purple for top layer 9, and light brown for internal layer 10.

The trends observed in Figure 4a and b allow us to hypothesize that the expansion and oxidation of the Li phase takes place in a continuous way from the top of the slab until the number of reactions decreases significantly. This behavior contrasts with the observed in Figure 4c and d, where for some layers the change in the Li atomic charge is progressive for some time and regressive in other times. This is attributed to the knock-off effect[89-90] where there is an exchange of position among Li atoms of different layers that allows Li atom diffusion to the top of the electrolyte phase.

Figure S2 illustrates the atomic electronic charge distribution in the Li-slab for systems 1 to 4. It shows that the dense phase remains practically unaltered and its charge is almost neutral. On the other hand, the porous phase has various degrees of oxidation of the Li atoms. At the bottom of the porous phase we find important presence of non-reacted solvent molecules. These molecules remain stable interacting with partially oxidized Li atoms with average charges of +0.3 |e|, while in the top porous phase there is a strong interaction among Li atoms and fragments from electrolyte molecules that dissociated (mainly F anions from $LiPF_6$ decomposition) forming a

representative group of organic and inorganic components that can be considered the initial SEI nuclei. The Li atoms that reach the top porous phase region are highly oxidized and get an average charge of +0.55 |e|. In summary, the further the Li-atoms migrate away from the slab the more oxidized they become, as shown by their more positive charges.

3.1.3. Li_xF coordination

In this section we analyze the interactions of the Li atoms with the different species present in each system and the initial stages of the SEI layer formation. The main SEI component obtained from the $LiPF_6$ salt systems is lithium fluoride (LiF), especially in cases where the main solvents used are more stable than the salt (for example DOL) and their decomposition is much delayed, although some of their initial decomposition products are detected and discussed. The time evolution of the Li_xF (x = 1, 2, 3, 4, 5, 6, 7+) was tracked and the results are summarized in Figure 5. Taking the F atom as a reference for the coordination, the ideal LiF crystal structure has six Li atoms for each F atom (for a periodic crystal the same could be said taking the Li atom as a reference and is surrounded by six F atoms). Figure 5 shows the evolution of the number of F atoms that reaches a specific Li coordination number along the simulation time. For Figure 5b and d the predominant coordination number is x = 5, i.e. the main component of the SEI is the Li_5F component. The Li_5F components interconnect among themselves and with other clusters with lower coordination. For the system with DME as solvent (Figure 5a) the coordination 5 is also predominant but there is an important presence of Li_6F clusters, while the system having DOL and FEC mixed as solvent (Figure 5c) shows a high tendency of the F atoms to reach the six coordination number, but also the LiF nuclei become more compact and someLi_7F are observed. Thus, a more compact and well-defined SEI appears, in contrast with the most amorphous one obtained from the previous cases. In general, the progressive increment in the coordination number can be understood by examining the behavior of some of the lines in Figure 5. For example, the low coordination Li_xF complexes (x = 1, 2, and 3) appear only in the early simulation times and the decrease in the fourth coordination is related with the increment in the fifth and sixth coordination in some cases. To complement Figure 5, Figure S3 summarizes the information of the pair radial distribution function (PRDF) for the Li-F pair in all four systems, where the average Li-F distance agrees with experimental reports.[91-92]

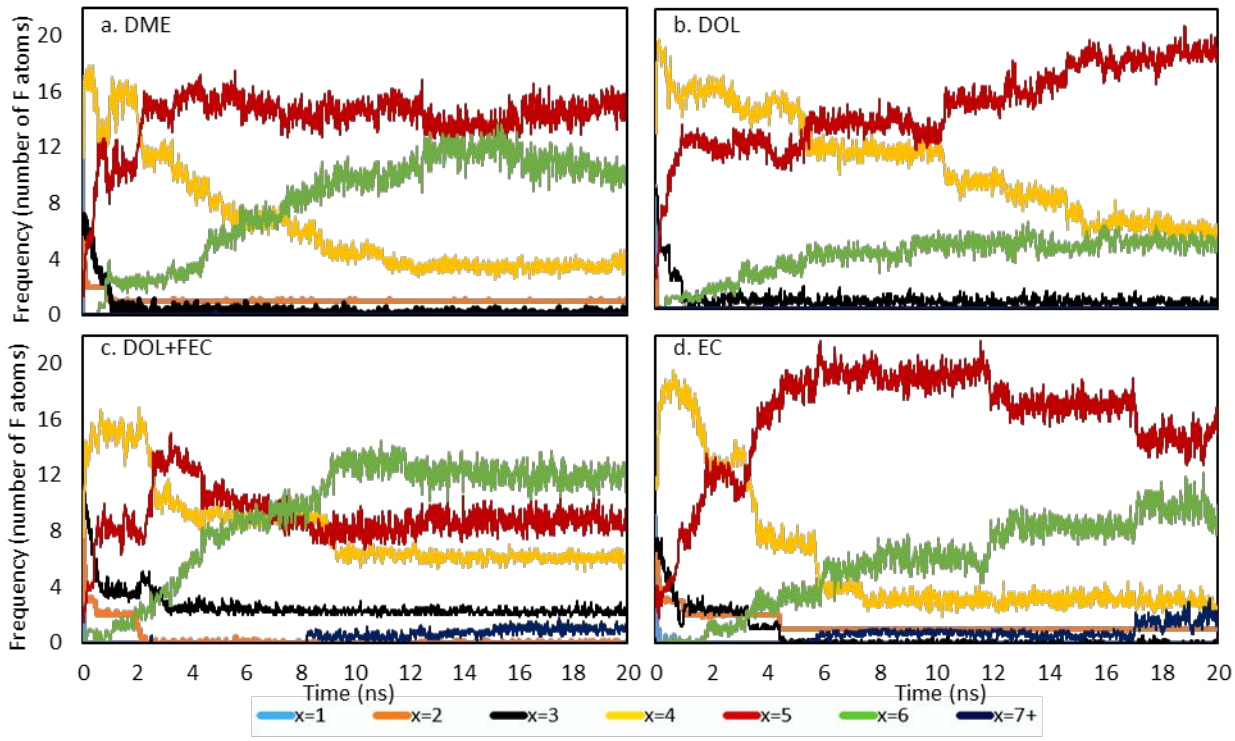

Figure 5. LixF coordination evolution for $LiPF_6$ in solvents evaluated: (a) DME, (b) DOL, (c) mix of DOL and FEC, and (d) EC. Color code: light blue for coordination x=1, orange coordination x=2, black coordination x=3, yellow for coordination x=4, red for coordination x=5, green for coordination x=6, and dark blue for coordination x=7 or higher.

3.1.4. F charge evolution

As the Li-slab atoms become oxidized, F atoms reach different charges according to their coordination number, and this feature brings specific electronic characteristics to the nucleating SEI. The charge evolution for the F atoms was followed up according to their coordination number reached during the simulation time. The information per F atom is shown in Figure 6. It is found that the higher the coordination number, the more negative the charge of the F atoms is. It makes sense since the ideal SEI should be stable among its constituents and oxidized Li atoms surrounding the F atoms have significant positive charge. Figure 6a and b show a smooth time dependent behavior compared with Figure 6c and d, where some charge evolution tendencies are more erratic. This agrees with the fact that a and b are the most stable systems. On the other hand, the high reactivity of molecules such as EC and FEC could bring additional charged fragments as a result of their reduction, so these phenomena affect the stability of the surrounding species and their charge evolution.

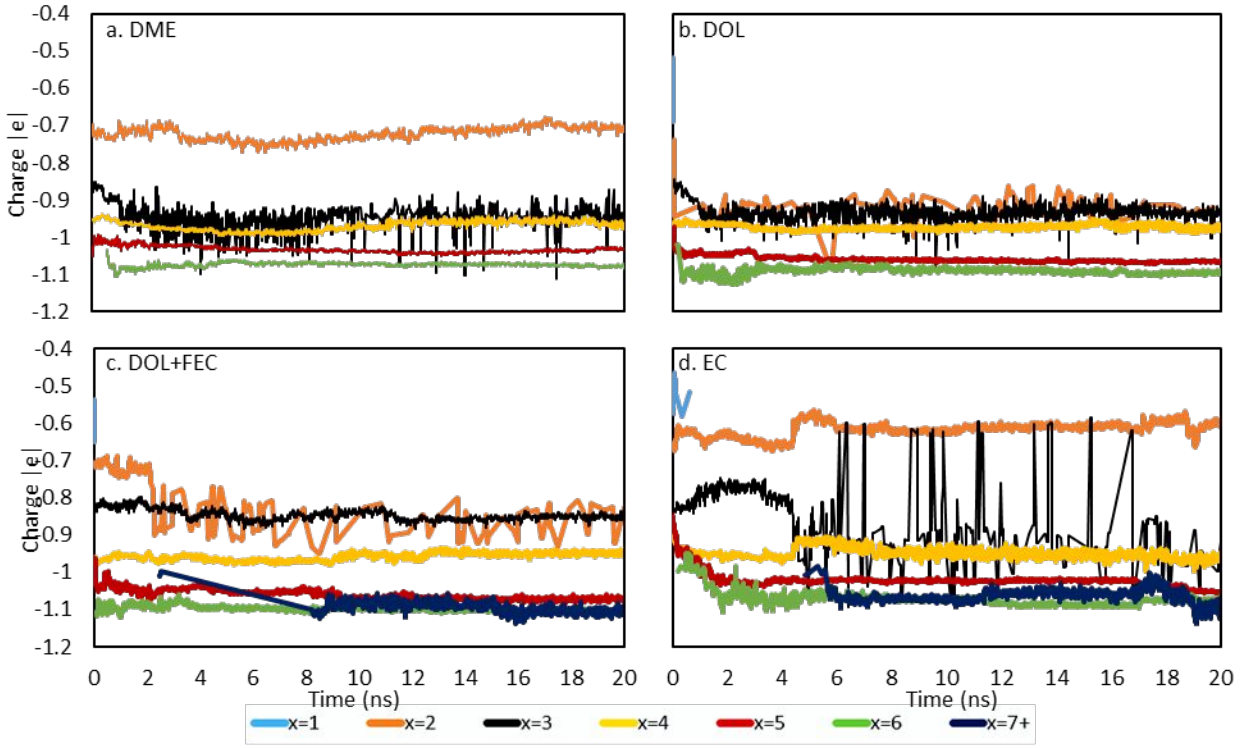

Figure 6. F atom charge evolution for LixF from $LiPF_6$ in different solvents evaluated: (a) DME, (b) DOL, (c) mix of DOL and FEC, and (d) EC. Color code: light blue for coordination x=1, orange coordination x=2, black coordination x=3, yellow for coordination x=4, red for coordination x=5, green for coordination x=6, and dark blue for coordination x=7 or more

3.1.5 LiF charge evolution

After looking at each SEI component individually, the analysis concentrates on the whole LiF and its characteristics. Figure 7 shows the average charge evolution for F and Li atoms that were tracked before in the coordination analysis, and the average charge of the whole LiF system during the simulation. For each one of the four cases, it can be seen how the SEI remains with a slightly negative charge, which could indicate the tendency for further growth. In these conditions, the SEI is mainly formed by LiF as F is the main component in $LiPF_6$ salt and the P atoms do not take a significant role in the products. The formed extended LiF network is amorphous but it reaches the theoretical LiF crystal coordination (i.e. the nucleating LiF hexa-coordinated crystal does not meet the angle specifications but is compact enough to reach the expected coordination for both F and Li atoms). The charge equilibration method is believed to bring reasonable approximations about electron exchange among the species[93-94] while solving the problem of assigning partial charges to atoms under constraints of charge neutrality into the systems,[77] however, to obtain more detailed information about charge transfer effects, more accurate methods are recommended.[44, 95-96]

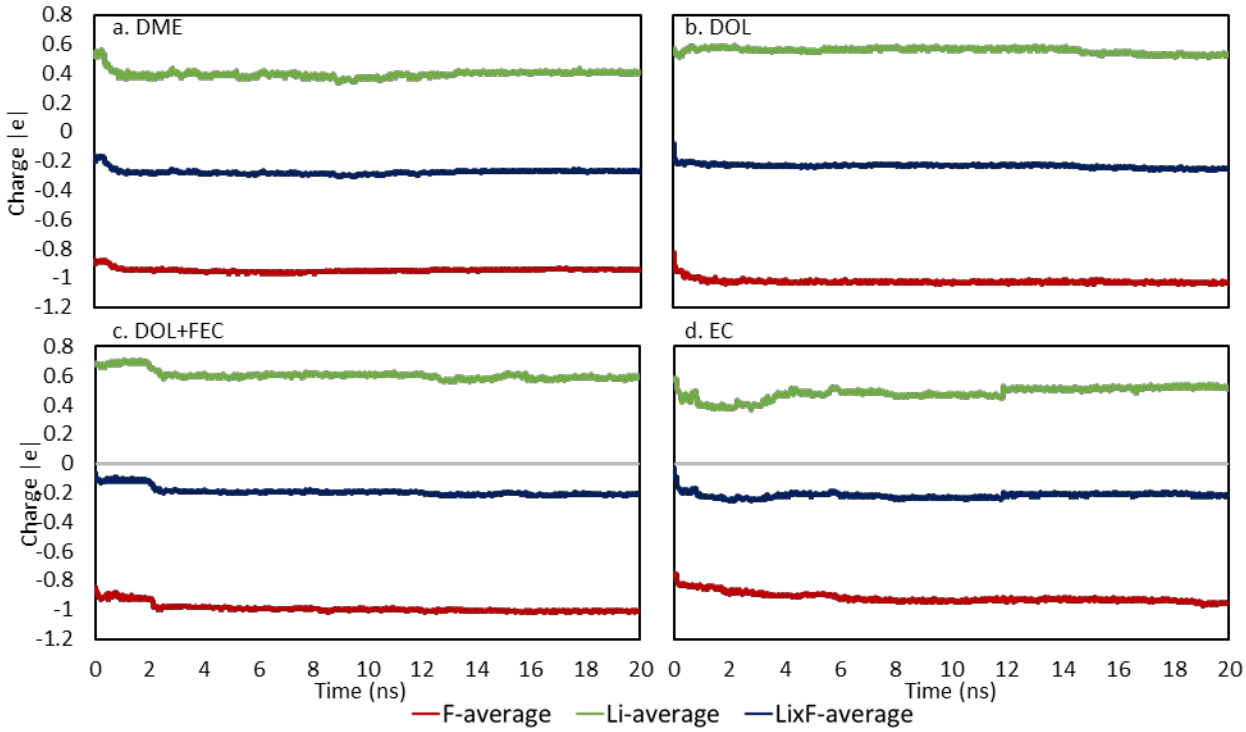

Figure 7. LiF charge evolution for SEI from $LiPF_6$ in different solvents evaluated: (a) DME, (b) DOL, (c) mix of DOL and FEC, and (d) EC. Color code: red for average F charge, green for average Li charge, and blue for average LiF charge evolution.

3.1.6 Formation of other inorganic and organic compounds

Due to decomposition of DME, FEC, and EC molecules, additional species result that may interact and form new components. Figure 8 summarizes the initial formation of lithium oxide fragments (Li_xO, x=1, 2, 3, 4) clusters owing to the reaction of Li with the oxygen atoms from the decomposed solvent molecules from reduction of DME, EC or FEC in each system. The stepped form of Figure 9c also matches with the times at which EC molecules decompose generating free O atoms. For both cases there is formation of carbon dioxide (CO_2) and ethylene (or ethene, C_2H_4), but in DOL+FEC system there is an important amount of vinyl fluoride (C_2H_3F). Previous work had shown the possibility of formation of VC-like fragments as one of the routes of FEC decomposition.[97] Figure S4 summarizes the pair radial distribution function for Li-O and Li-C pairs showing relatively weak interaction between these atomic species.

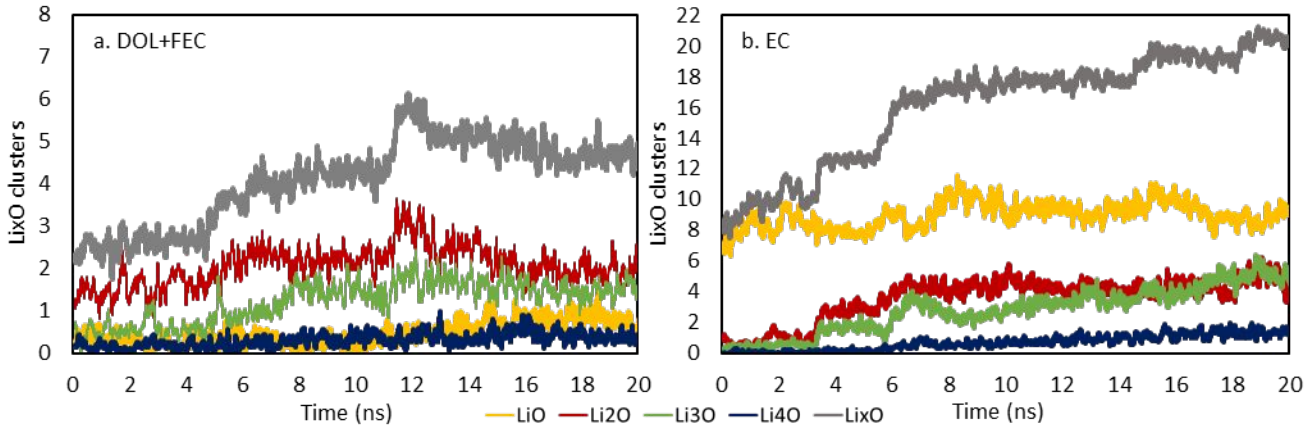

Figure 8. Formation of lithium oxide clusters LixO (x =1 to 4) with different oxygen coordination for the systems with (a) mixture of DOL and FEC as solvent and (b) EC as solvent. Color code: yellow for LiO, red for Li_2O, green for Li_3O, blue for Li_4O, and gray for the total amount of lithium oxide clusters (LixO).

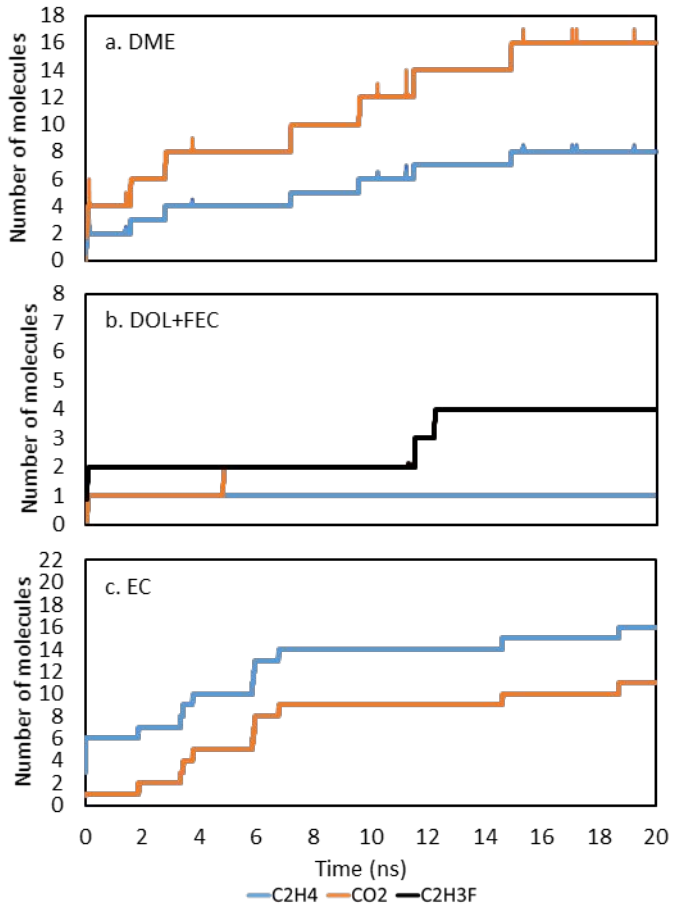

Figure 9. Formation of organic species for the systems with (a) mixture of DOL and FEC as solvent and (b) EC as solvent. Color code: blue for ethylene (or ethene, C2H4), orange for carbon dioxide (CO_2), black for vinyl fluoride (C_2H_3F), and gray for the total amount of lithium oxide clusters (LixO).

3.2 Systems 5 to 8: Electrolyte based on LiTF solutions

In general terms, the behavior of systems with $LiPF_6$ is comparable with those having LiTF as a salt. But is important to track the main differences. The first general difference can be observed when comparing Figure S5 with Figure 1. Figure S5 shows a more complex atomic charge distribution and SEI structure due to the interaction of new species that decompose from the LiTF salt (i.e. there are relatively high amounts of C, S and O that participate actively in the formation of the SEI). Comparatively, the amount of LiF is much lower.

3.2.1. Li-slab expansion

Li-slab expansion (Figure S6) shows the same general trend in all 5 to 8 systems (see Table 1 for detailed composition). Nevertheless, some differences compared to the $LiPF_6$ results are related with the rate at which the Li-slab expands and the behavior of the lower blocks. For all systems in Figure S6, block number seven expands toward the top region of the systems, as demonstrated in the reduction of density, while blocks eight and nine (the bottom section of the slab, representing the "bulk" behavior) remain almost unaltered keeping the bulk structure (see Figure 1a for numbering of the blocks). This expansion takes place in a relatively short time, especially for the mixture of DOL and FEC solvents and for the EC solvent-based system. On the other hand, comparing Figure S6 with Figure 2 for the $LiPF_6$ cases, block seven tends to have slightly higher density, indicating that the top layers tend to expand not only toward the top but also slightly to the bottom region. The behavior for the total density is comparable between Figures S1 and S7, where in the top blocks the total density (including Li and all the other components) remains high due to the accumulation of non-reacted solvent molecules and the formation of the SEI.

3.2.2. Li charge evolution

Although Figure S8 seems to be noisy, it brings really important information when compared with Figure 4 for $LiPF_6$ systems. First point to highlight is that in LiTF systems all the top ten Li-slab layers oxidize from the beginning of the simulations. It is indicative of how reactive these systems are. As discussed later, some components seem to have preferential locations, causing the main reactions to be located in other regions than the one initially occupied only by the electrolyte. This can be observed in Figure S9, which shows the configuration reached after the Li-slab expansion during 20 ns of simulation time for systems 5 to 8 with LiTF as salt. The general behavior is the same as discussed for $LiPF_6$, with the different porous Li regions being identified. Presence of light color atoms in the bottom of the slabs corresponds to O atoms forming lithium oxide clusters in that region, where the Li atoms keep the slab structure and the O atoms can reach their preferential coordination located in the interstitial spaces.

3.2.3. SEI formation in systems with LiTF

Even though the main component of the SEI in systems with LiTF salt is LiF, there is also relevant presence of some other components derived from salt decomposition. For LiF formation, Figures S10a to d show a predominant coordination of six Li atoms per F atom and an increasing amount of F atoms coordinated with seven or more atoms, illustrating how the SEI becomes more compact. For cases where solvent is (a) DME, (b) DOL, and (c) DOL and FEC mixture in Figure S10 the F coordination with one Li atom only lasts for short time (as can be seen also in the charge evolution in Figure S12), and for the case of DOL, even the coordination two disappears in a relatively short simulation time. Figure S11 shows the PRDF for the Li-F pair system. This graph shows almost similar behavior as Figure S3. The shape of the DOL-based curve may suggest the formation of a more compact SEI. On the other hand, the F atom charge evolution for LixF from LiTF in the various solvents evaluated shows a smooth evolution, as shown in Figure S12. In general, the charge evolution behavior is similar in presence of both $LiPF_6$ and LiTF, both in the functional form and in the range of atomic charges.

3.2.4. SEI charge evolution

As stated before, in all systems with LiTF we have other species forming the SEI instead of only LiF as with $LiPF_6$. In these cases, the components evolving from salt as well as some electrolyte molecules decomposition bring special characteristics to the SEI layer. Starting with the main SEI component, Figure S13 summarizes the average atomic charge for F and Li species and for the LixF compounds of the SEI. All four cases are comparable with the ones derived from $LiPF_6$ in Figure 7. The average atomic charge for LixF-SEI species remains with a similar negative charge as in the former cases. This indicates again the possibility for further interaction with surrounding species which allows for SEI growth.

Analyzing the interactions among other species brings new insights regarding the role of the nature of the salt present in the system for defining the SEI formation pathways or properties. Here we look at other components based on Li-S, Li-C, S-C, and Li-O pairs. Figure S14 summarizes the PRDFs for these pairs. For some specific systems the interaction between these pairs of species is stronger than in others, with considerably closer bonding distances. Figure 10 depicts the coordination evolution for S atoms (i.e. the formation of Ψ_xS species, where Ψ may be mainly -Li or some -C based component). The main S-based component present is Li_xS, and the coordination evolution graph shows a great preference for the coordination x=6, 7, and 8. This suggests 6, 7, 8 Li atoms surrounding one S atom, which could be precursor of a Li_2S structure formation. The charge evolution per S atom summarized in Figure S15 demonstrates

that -S components with coordination x=6, 7, and 8 are the most stable compared with other coordinations, as these have smoother tendencies and keep the behavior previously noted in the LixF compounds (the larger the coordination number the more negative the atomic charge of the S atom). Following the same analysis for the LixF-SEI formation, Figure 11 depicts the Ψ-S-SEI charge evolution, showing almost neutral charge with low negative value for cases with DME, DOL and FEC, and EC, and an interesting behavior for DOL where most of the simulation time the Ψ-S-SEI charge switches from positive to negative.

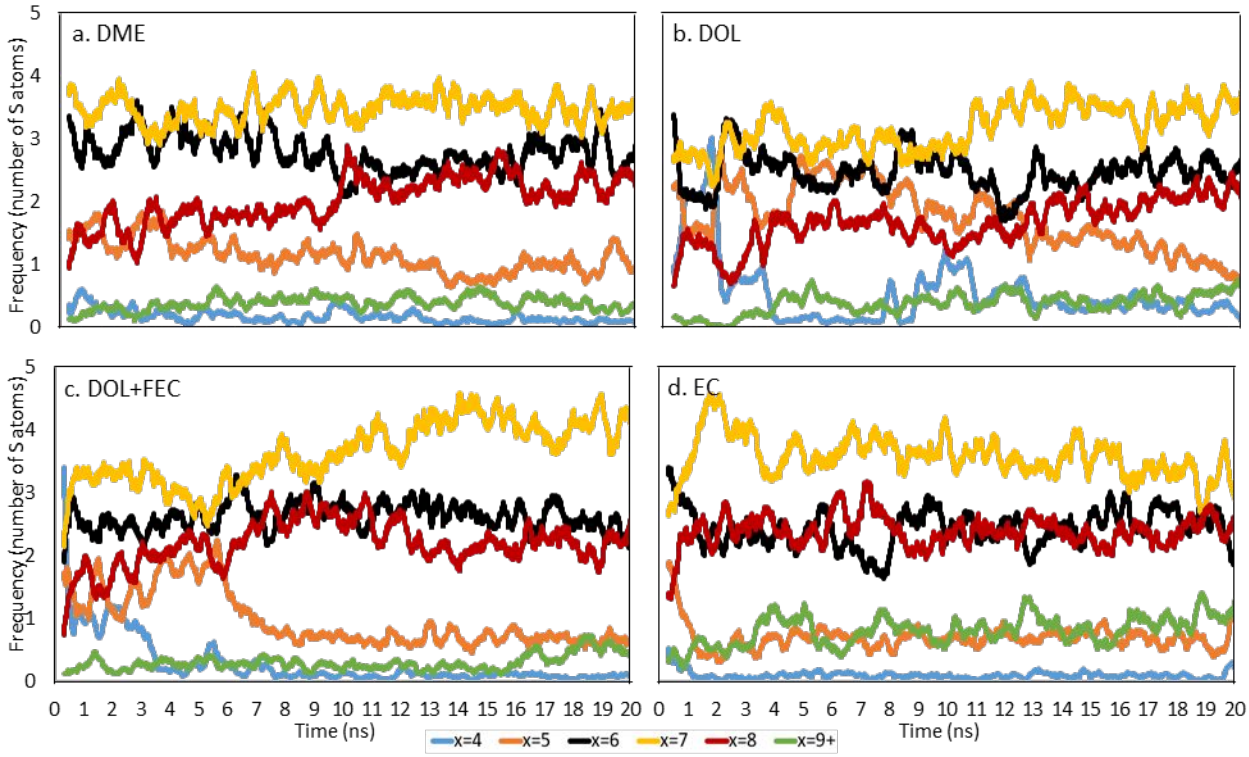

Figure 10. Ψ_xS coordination evolution for LiTF in different solvents evaluated: (a) DME, (b) DOL, (c) mix of DOL and FEC, and (d) EC. Color code: light blue for coordination x=4, orange coordination x=5, black coordination x=6, yellow for coordination x=7, red for coordination x=8, and green for coordination x=9 or more. Here Ψ is mostly Li.

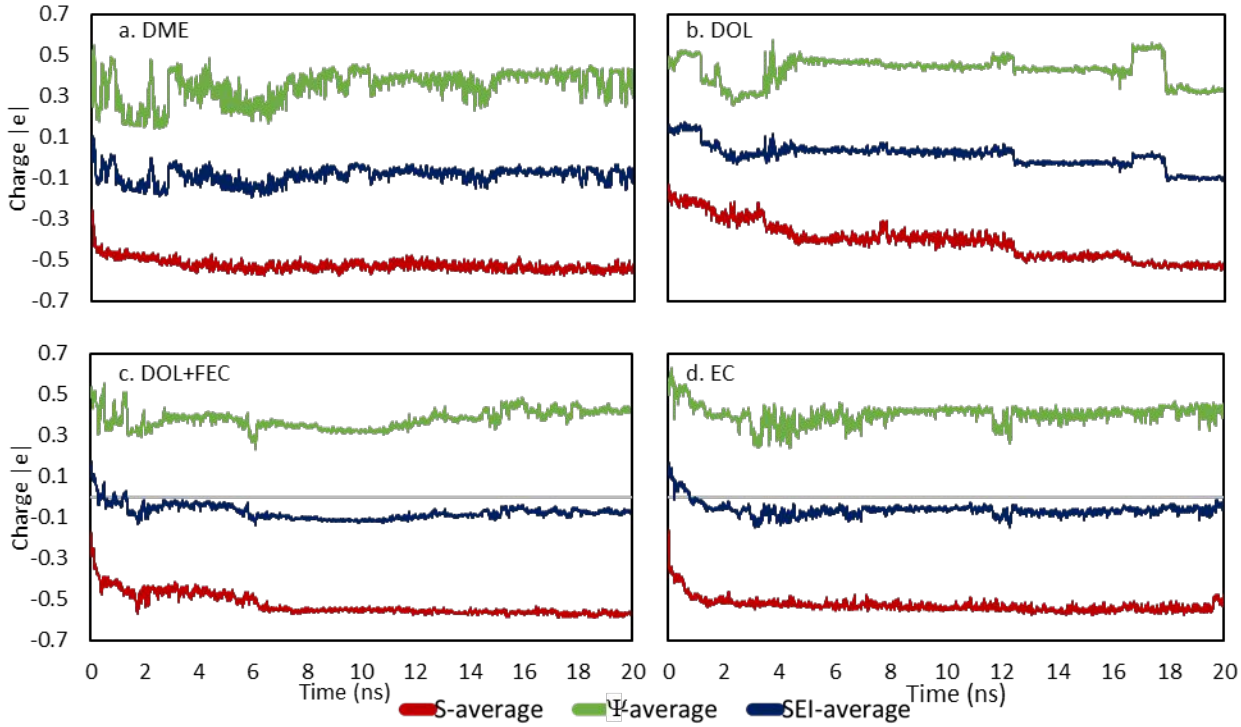

Figure 11. Ψ_xS-SEI charge evolution for SEI from LiTF in different solvents evaluated: (a) DME, (b) DOL, (c) mix of DOL and FEC, and (d) EC. Color code: red for average S charge, green for average Ψ-species charge, and blue for average SEI charge evolution. Here Ψ is mostly Li.

Other important species are the C atoms that are incorporated into the SEIs both from salt and solvent decomposition. Tracking C behavior is important after detecting other species that can react with C atoms (e.g. Li, O, and also H or other C atoms). Following the evolution of free C atoms we found that its behavior is not uniform among the various electrolytes. Figure 12 shows the coordination evolution for the C atoms that are free in each system. High coordination numbers (i.e. x=4 and 5) are relatively frequent, suggesting that C species act similarly in different electrolytes. In contrast, analyzing Figure S16 and the charge evolution for C atoms reacting in each one of the systems, its behavior seems to highly depend on its surrounding environment and the nature of its interacting species, especially if following the charge evolution for lower coordination (i.e. x=3 and 4).

Similar patterns are detected for the Ψ-C-SEI formed as shown in Figure 13, especially for DOL and EC, where for the first case the charge evolution shows an erratic behavior at the early simulation times, while for the second one a smooth evolution changes in the last part of the simulation due to a sudden loss of electrons in the C atoms. Even though, the general observation is that the C species brings a considerable negative structure to the whole SEI, and as stated before in this discussion, this can lead the SEI to grow more if there are plenty of surrounding species to interact and react with.

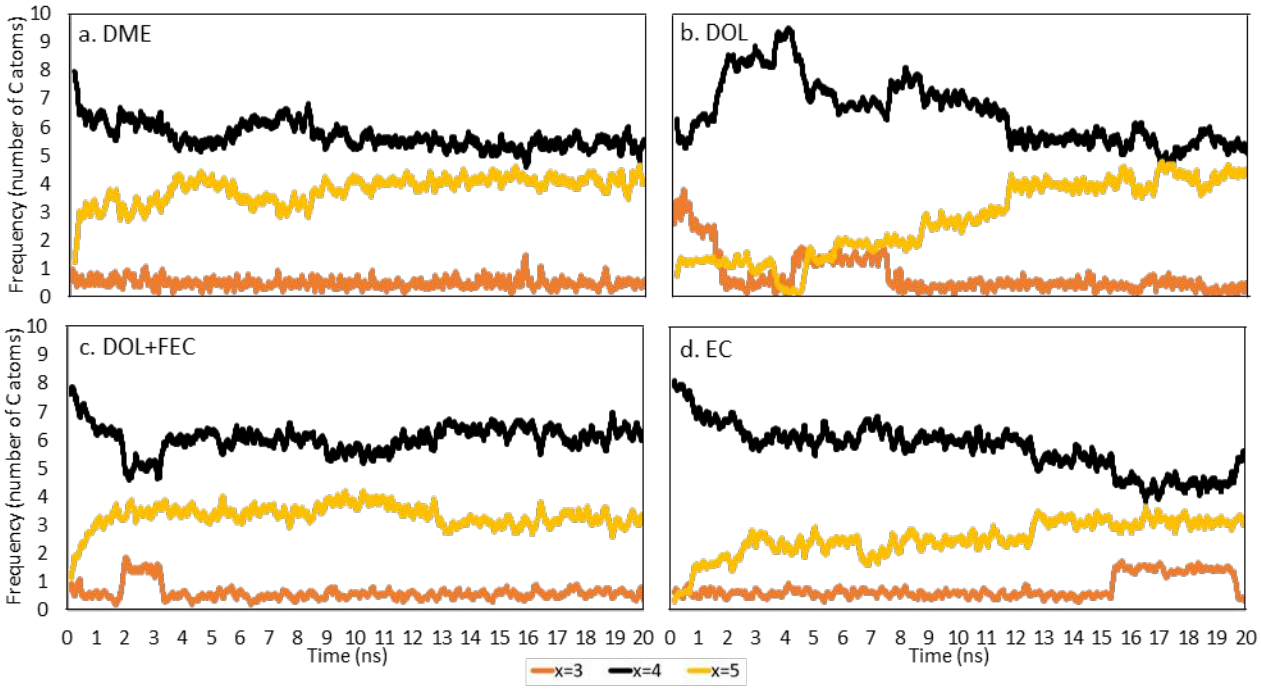

Figure 12. ΨxC coordination evolution for LiTF in different solvents evaluated: (a) DME, (b) DOL, (c) mix of DOL and FEC, and (d) EC. Color code: orange coordination x=3, black coordination x=4, and yellow for coordination x=5. Ψ may be mostly species Li or some species S.

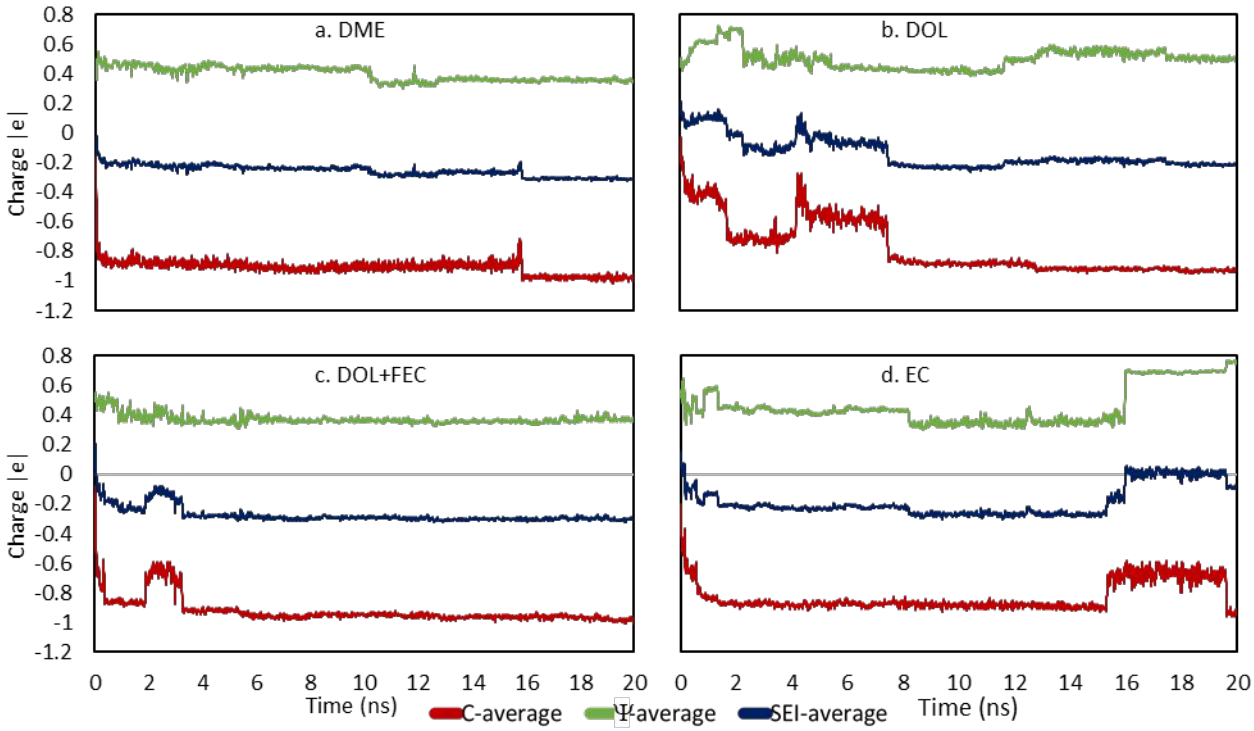

Figure 13. Ψ_xC-SEI charge evolution for SEI from LiTF in different solvents evaluated: (a) DME, (b) DOL, (c) mix of DOL and FEC, and (d) EC. Color coding: red for average C charge, green for average Ψ-species charge, and blue for average SEI charge evolution.

Finally, lithium oxide is another important component present in the LiTF-based SEIs. For these systems where there are more species available to form different compounds, there is no major presence of organic compounds, and neither CO_2 nor C_2H_4 are formed. Figure S17 shows the formation of species for (a) DME and (b) EC. In the first case methoxide groups (CH_3O) and LixO are formed, and for the second case there is formation of CO_2 and LixO. LixO (x=1, 2, 3, and 4) is formed in an important amount and as stated in Figure S9, its preferential formation site is the bulk structure of the lithium slab (i.e. the bottom layers that keep the bulk structure and density). The formation of LixO (x=1, 2, 3, and 4) clusters along time is found in Figure 14. Li_2O and Li_3O are the predominant compounds. Analyzing their distribution in the slab, there is no interconnection between clusters that allows further formation of complex compounds such as peroxide.

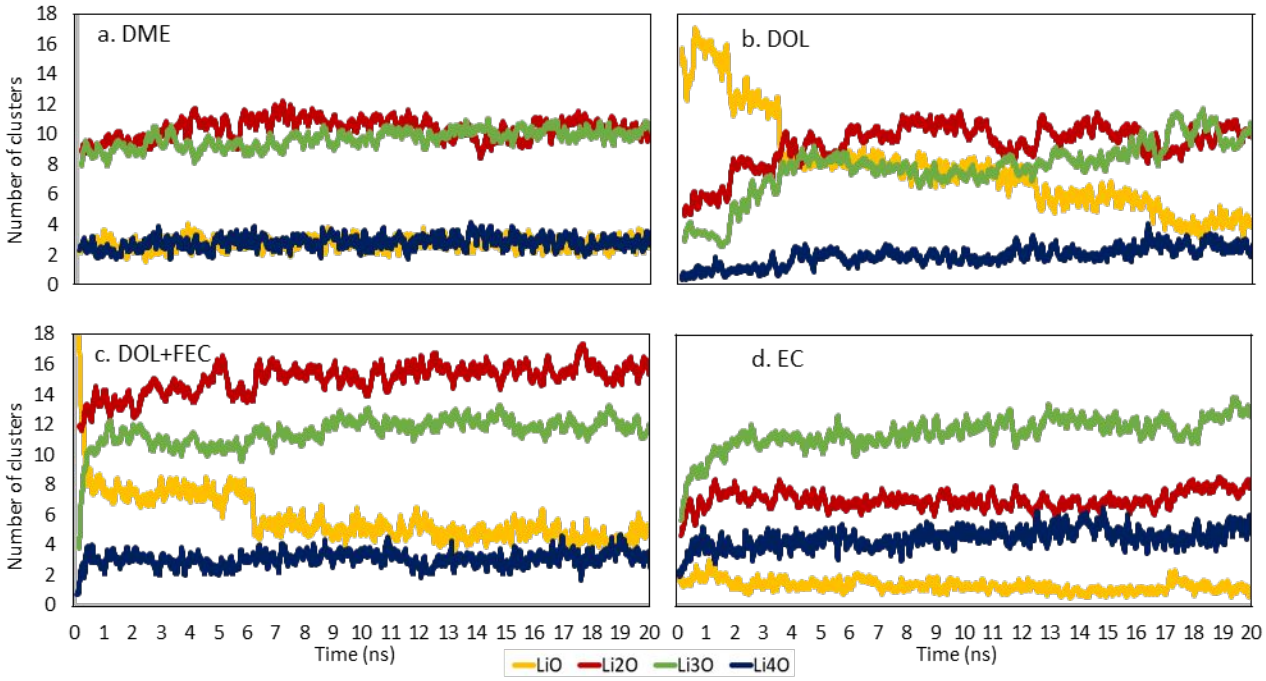

Figure 14. Formation of lithium oxide clusters with different oxygen coordination for systems containing the following solvents (a) DME, (b) DOL, (c) mix of DOL and FEC, and (d) EC. Color code: yellow for LiO, red for Li_2O, green for Li_3O, and blue for Li_4O.

3.2.5. SEI structure

Specific SEI properties and morphology are crucial for the desired battery performance. In this work, we were able to follow the formation of the SEI structure in eight different systems and compare them. Figure 15 andFigure 16 depict the SEI structure for systems with $LiPF_6$ and LiTF, respectively, and the Li-slab configuration after 20 ns. In these figures, all other components (i.e. unreacted electrolyte molecules and other organic gas compounds as CO_2 or C_2H_4) are shown as wireframe structures for a better visualization of the SEI. In Figure 15b and d the dispersed O atoms are product of electrolyte decomposition, as discussed earlier, and at the top of Figure 15c some unreacted FEC molecules are observed. The front view in Figure 15, compared with the orthogonal view in Figure S18 for the same systems brings an insight on the SEI distribution in the simulation cell. For both pure DOL and DOL mixed with FEC the SEI appears to be agglomerated at specific positions of the cell, while for both the DME and EC systems the SEI seems to be more distributed in the XY-plane, forming an amorphous layer. On the other hand, comparing Figure 16 and Figure S19 one can observe the preferential formation site for the different SEI components. For (a) DME, (c) DOL and FEC, and (d) EC it is clear how the free O atoms fill almost all the space in the dense phase, but not in (b) pure DOL system. However, in DOL, lithium oxide clusters form in lower locations compared with other components, so it keeps the tendency although at a different rate of formation/diffusion to the bottom of the cell. Although in LiTF systems there are more species available to form the SEI, the structure appears more amorphous than in the previous cases, being formed as compact nuclei but not as a layer. Figure S20 and Figure S21 show the atomic charge distribution for Li-slab atoms and SEI

compounds. Even though the SEI atomic charge ranges for both $LiPF_6$ and LiTF are similar, their distribution is considerably different, which implies distinctive performance for each case.

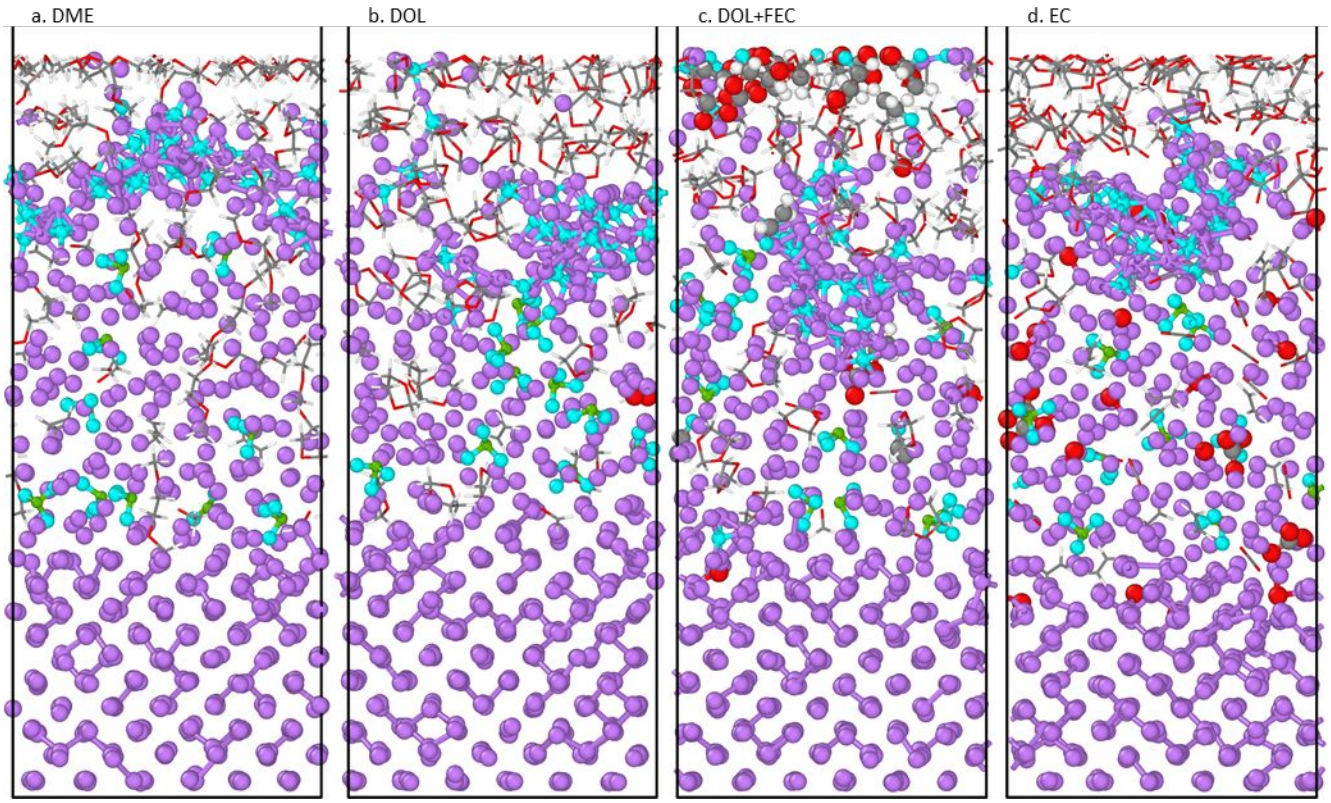

Figure 15. Front view for the SEI formed from $LiPF_6$ in liquid electrolyte (a) DME, (b) DOL, (c) DOL mixed with FEC, and (d) EC. Wireframe structures correspond to unreacted electrolyte molecules and other organic compounds for better visualization. Color code: light blue for F, red for O, purple for Li, white for H, gray for C, and green for P.

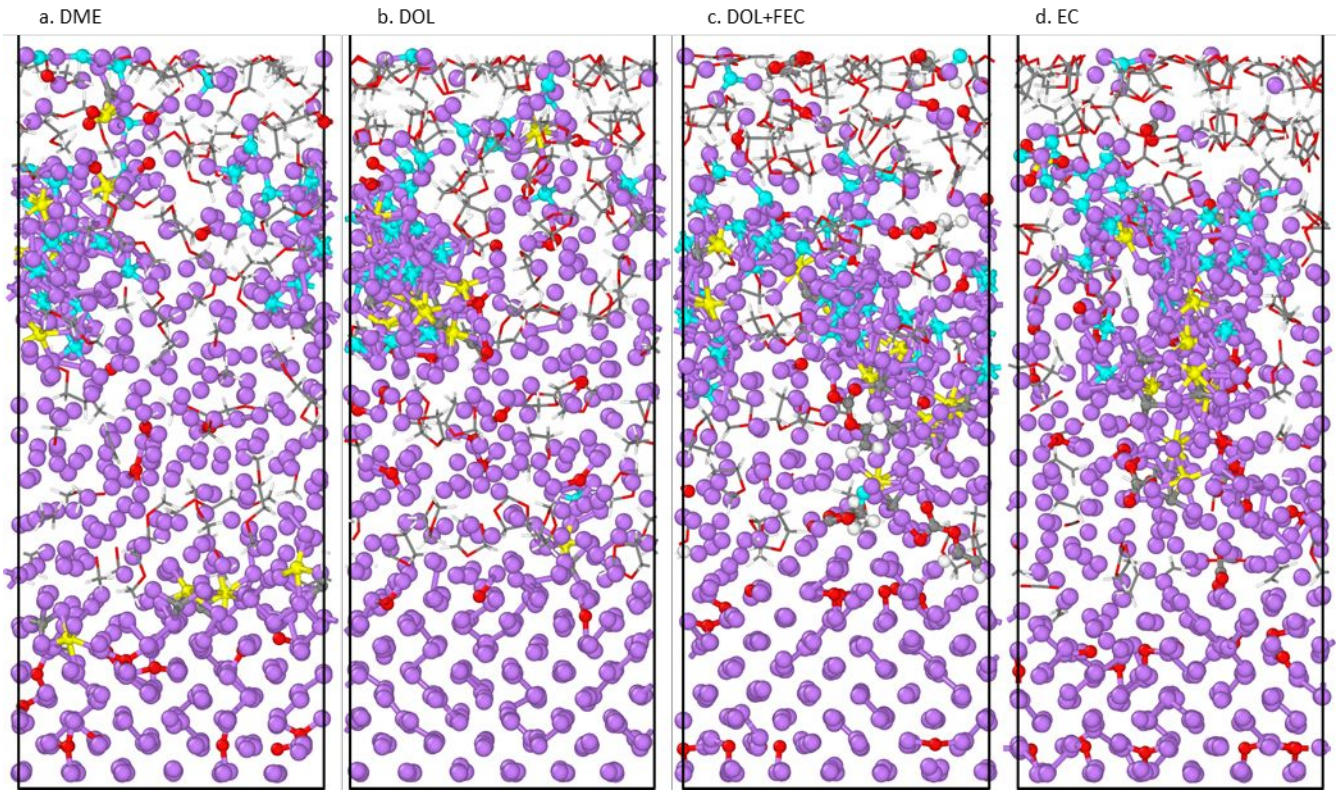

Figure 16. Front view for the SEI formed from LITF in liquid electrolyte (a) DME, (b) DOL, (c) DOL mixed with FEC, and (d) EC. Wireframe structures correspond to un-reacted electrolyte molecules and other organic compounds for better visualization. Color code: light blue for F, red for O, purple for Li, white for H, gray for C, and yellow for S.

3.3 SEI fragments and clusters

In this section we analyze the formation of LixF clusters using quantum chemistry calculations on the basis of the observations from MD simulations.

3.3.1 SEI fragments

Following the sequential addition of Li atoms/ions to a fluorine anion in cluster DFT calculations, the highest coordination number reached is 4 (Li_4-F). Extra lithium atoms or ions added to the system will no longer be bonded to the fragment since it becomes thermodynamically unfavorable. When an initial guess of a larger fragment (Li_{n+4}-F) is optimized in cluster DFT calculations using Gaussian16, the optimization algorithm breaks the extra bonds postulated and falls back to reactant state. This is also observed in MD where some of the small individual Li-F fragments are not able to achieve maximum coordination of 6. However, coordination of 6 can be observed in MD among large clusters once the nucleation process begins. Table 2 shows the reaction energies of fragment formation.

Table 2: Calculated Li_x-F (x =2, 3, 4) fragment formation reaction enthalpies and free energies

	Reaction	ΔH_{reax} (kJ/mol)	ΔG_{reax} (kJ/mol)	Normalized ΔH_{reax} (kJ/mol) per Li	Normalized ΔG_{reax} (kJ/mol) per Li
1	$LiF + Li \rightarrow Li_2F$	-74.667	-49.942	-37.334	-24.971
2	$Li_2F+Li \rightarrow Li_3F$	-85.229	-58.848	-28.410	-19.616
3*	$Li_3F + Li \rightarrow Li_4F$	-94.437	-62.671	-23.609	-15.668
4	$LiF^{1-} + Li \rightarrow Li_2F^{1-}$	-102.384	-72.821	-51.192	-36.411
5	$Li_2F^{1-} + Li \rightarrow Li_3F^{1-}$	-58.299	-30.574	-19.433	-10.191
6	$Li_3F^{1-} + Li \rightarrow Li_4F^{1-}$	-74.365	-43.266	-18.591	-10.817

The optimized geometry of each fragment and their electrostatic potential are included in the Figures S22 and S23. One thing to note is that for reaction #3, the resulting fragment (neutral Li_4F) has an unusual elongated bond between the fourth Li and F. However, its counterpart Li_4F^{-1} displays no such characteristics. It might seem like Li_4F fragment is at its reactant stage, and the bond between the 4th Li and F is not formed. However, based on frequency calculations, this configuration is confirmed to be at ground state, and its energy is also far lower than the sum of separate reactants. Furthermore, the calculated atomic polar tensors [98] (APT) charges show that the fourth lithium has a slightly negative charge, which might only be a result of redistributing the electron density of the entire fragment. The electrostatic potential surface also shows two electron-rich sites between the 4th lithium and the fluorine atom, further proving the existence of a 4th Li-F interaction. Combining all these evidences, we can validate this Li_4F configuration. The need of the addition of the negative charge in reactions 4-6 also follow the behavior observed in the MD simulations discussed above.

3.3.2 SEI clusters

The initial LiF nucleation process is simulated by joining two fragments together with mutual bonds to a pre-existing Li atom. Table 3 shows the energies of forming a two-fragment cluster. The optimized geometry of each cluster and their electrostatic potential are included in the Figures S24 to S26. It should be noted that only Li_3F and Li_4F clusters with different charges are considered in the formation of clusters. Based on observations from MD simulations, we made

the general assumption that LiF and Li_2F fragments are more likely to receive additional Li rather than forming a cluster. High electron density near the shared Li atom is a common characteristic for all LiF clusters. All reaction energies of clustering are favorable except for reaction 6. The endergonic nature of this reaction can again be explained by its doublet state. When attempting to combine two relatively large fragments (Li_4F and Li_4F^-), the unpaired electron leads to relative high energy.

Table 3: Energies of forming two-fragment clusters

	Reaction	ΔH_r(kJ/mol)	ΔG_r(kJ/mol)
1	$Li_3F + Li_3F \rightarrow Li_3F \bullet Li_3F$	-142.767	-81.855
2	$Li_3F + Li_4F \rightarrow Li_3F \bullet Li_4F$	-135.256	-73.622
3	$Li_4F + Li_4F \rightarrow Li_4F \bullet Li_4F$	-148.527	-79.130
4	$Li_3F^- + Li_3F \rightarrow (Li_3F \bullet Li_3F)^-$	-95.707	-50.906
5-a	$Li4F^- + Li_3F \rightarrow (Li_3F \bullet Li_4F)^-$	-239.099	-178.19
5-b	$Li_3F^- + Li_4F \rightarrow (Li_3F \bullet Li_4F)^-$	-219.207	-158.785
6	$Li_4F^- + Li_4F \rightarrow (Li_4F \bullet Li_4F)^-$	-178.791	-118.793
7	$Li_3F^- + Li_3F^- \rightarrow (Li_3F \bullet Li_3F)^{2-}$	-254.364	-204.398
8	$Li_3F^- + Li_4F^- \rightarrow (Li_3F \bullet Li_4F)^{2-}$	-212.085	-163.088
9	$Li_4F^- + Li_4F^- \rightarrow (Li_4F \bullet Li_4F)^{2-}$	-223.325	-167.945

In order to check if the basis set superposition correction energy (BSSE) was significant in this type of simulations, we have run several simulations with a larger basis set (aug-cc-pvtz). Due to very small differences (less than 5 kJ/mol) found for all these simulations, we concluded that BSSE correction energy is not significant enough to impact our original results.

3.4 How are these findings related to previous computational and experimental studies

Our results enrich a growing computational literature on the SEI topic, including reviews on modeling SEI formation and growth,[99] interfacial phenomena[100], and multiscale modeling of energy materials,[101] first principles understanding of ion electrodeposition,[102] charge transfer through the SEI,[103] effects of electric field on battery transport and reactivity,[64, 104-114] among others. However, our analysis of the nucleation and growth of the SEI components provides new

additional insights into a less understood topic that is the nucleation and growth of native SEIs on Li metal.

On the experimental side, numerous technological advances have allowed in recent years the experimental investigation of the initial stages of SEI growth. Among them, cryogenic scanning transmission electron microscopy (cryo-STEM) along with X-ray photoelectron spectroscopy (XPS) and secondary ion mass spectrometry (SIMS) are especially useful to identify nanoscopic SEI components.[115] Interestingly, recent work that employed a combination of these techniques reported similar SEI structures as those shown in our study.[116] In particular, similarly to our findings, the authors identified a combination of Li_2O and LiF structures as the main SEI components from a $LiPF_6$ based electrolyte in a mixture of carbonate solvents. The partial oxidation of the Li surface layers was also characterized by cryo-STEM. [117] The formation of LiF nanostructures discussed from our simulations was also followed by *ex-situ* XPS analysis.[118] Other work explored the importance of the formation of polymeric species due to the presence of additives such as fluoroethylene carbonate (FEC) [119], that is also in agreement with our findings of precursors for polymerization in similar solutions. Our results comparing different salts supports recent analyses based on tuning the anion chemistry [120] for obtaining specific SEI components. Our work also contributes to clarifying the role of the solvent on stabilizing SEI structure, that is another current topic of investigation as demonstrated in experimental studies.[121] The main advantage that we would like to highlight is that the theoretical/computational tool allows the detailed analysis of the reactivity and the evolution of initial nucleation and growth that definitely complements and clarifies the results of modern surface science techniques.

4. Conclusions

The formation of a “native” spontaneously formed SEI due to the interactions of a Li metal surface with a liquid electrolyte is studied using classical molecular dynamics simulations and a reactive force field. Two salts are used in 2M solutions of various solvents and mixtures of solvents. The analysis of Li-slab expansion shows that the Li porous phase starts forming almost instantaneously from the beginning of the simulation, due to oxidation of the surface Li atoms in contact with the electrolyte and proceeds during the complete computational experiment lasting 20 nanoseconds. At the end of the simulation, not all the Li metal phase is consumed; the bottom layers remain intact with an average density close to that of Li metal, 0.53 g/cc. Simultaneously with Li oxidation, electrolyte reduction takes place. First, reduction reactions produce atoms and fragments that are separated from their respective molecules (usually as anions or radical anions) and interact with the partially oxidized Li atoms, forming nuclei for the various SEI components:

LiF, Li oxides, organic molecules (some of them precursors for polymerization), and nuclei for compounds derived from S and C. The chemistry and characteristics of the SEI phase depend on the original electrolyte (salt/solvent). Details are obtained from post-processing of the data from the dynamic trajectories. It is found that the rate of formation of the Li_6F, LixO, and LixS nuclei that are precursors for crystalline LiF, Li-oxides and Li_2S phases depends strongly on the composition of the electrolyte. Very interesting differences are observed regarding the rate of formation of the individual products as a function of salt type, and solvent composition. Although for both salts the main product is LiF, the nucleation of LiF is different due to the characteristic reactive environment in each case. For $LiPF_6$ solutions, besides LiF, some organic products are detected from solvent decomposition. However, the organic phase has a slower kinetics of nucleation and growth and only fragments and very initial agglomeration is detected in this timeframe. For the LiTF phase, besides the dominant LiF, fast diffusion of O and S atoms (usually negatively charged) takes place. As a result, both atoms pair with Li ions and start forming their respective oxide and sulfide products.

Partially oxidized Li ions moving from the metal phase toward the electrolyte phase are observed to move via a knock-off mechanism, [122] but the exchange of atoms does not affect the formation of different regions, specially the dense phase that keeps the slab structure. Instead of a layer, the SEI is formed as an amorphous bulk structure close to the top region of the simulation cell. In between the SEI and the Li metal there is a continuously reacting porous phase. However, the distribution of reacting nuclei depends strongly on the nature and composition of the electrolyte. This uneven distribution of the SEI compounds could lead to preferentially uneven lithium deposition upon battery charge. However, understanding the early processes discussed here is crucial to elucidate more complex phenomena occurring during battery cycling. Future work will address many other aspects that will help understanding the subsequent stages of simultaneous SEI growth and Li deposition, and also additional events occurring during Li stripping.

Supporting Information

The following information is available and cited/described in the text. For $LiPF_6$-based systems: Total density evolution (S1), charges Li phase (S2), RDFs (S3, S4); For LiTF-based systems: Initial and final configurations (S5), Li density evolution (S6), Total density evolution (S7), Charge evolution Li layers (S8), Charges in Li atoms (S9), LixF evolution (S10), RDFs (S11, S14), Charges F (S12, S13), Charges S (S15), Charges C (S16), Organic species evolution (S17), SEI structure (S18, S19), Charge distribution SEI (S20, S21), optimized negatively charged LixF

fragments (S22, S23, S24), Optimized neutral LixF clusters (S25), Clustering LixF (S26), Electrostatic potentials LixF (S27 and S28).

Conflicts of Interest

There are no conflicts of interest to declare.

Acknowledgments

This work was supported by the U.S. Department of Energy's Office of Energy Efficiency and Renewable Energy (EERE), as part of the Battery 500 Consortium, Award Number DE-EE0008210. Supercomputer resources from the Texas A&M University High Performance Computer Center, and Texas Advanced Computing Center (TACC) are gratefully acknowledged.

References

1. Jacobson, M. Z.; Delucchi, M. A., Providing all global energy with wind, water, and solar power, Part I: Technologies, energy resources, quantities and areas of infrastructure, and materials. *Energy Policy* **2011,** *39* (3), 1154-1169.
2. McGlade, C.; Ekins, P., The geographical distribution of fossil fuels unused when limiting global warming to 2 °C. *Nature* **2015,** *517*, 187.
3. Yang, Z.; Gu, L.; Hu, Y.-S.; Li, H., Atomic-Scale Structure-Property Relationships in Lithium Ion Battery Electrode Materials. *Annual Review of Materials Research* **2017,** *47* (1), 175-198.
4. Etacheri, V.; Marom, R.; Elazari, R.; Salitra, G.; Aurbach, D., Challenges in the development of advanced Li-ion batteries: a review. *Energy & Environmental Science* **2011,** *4* (9), 3243-3262.
5. Armand, M.; Tarascon, J. M., Building better batteries. *Nature* **2008,** *451* (7179), 652-657.
6. Goodenough, J. B.; Kim, Y., Challenges for Rechargeable Li Batteries. *Chemistry of Materials* **2010,** *22* (3), 587-603.
7. Choi, N.-S.; Chen, Z.; Freunberger, S. A.; Ji, X.; Sun, Y.-K.; Amine, K.; Yushin, G.; Nazar, L. F.; Cho, J.; Bruce, P. G., Challenges Facing Lithium Batteries and Electrical Double-Layer Capacitors. *Angewandte Chemie International Edition* **2012,** *51* (40), 9994-10024.
8. Goodenough, J. B.; Kim, Y., Challenges for rechargeable batteries. *Journal of Power Sources* **2011,** *196* (16), 6688-6694.
9. Thackeray, M. M.; Wolverton, C.; Isaacs, E. D., Electrical energy storage for transportation—approaching the limits of, and going beyond, lithium-ion batteries. *Energy & Environmental Science* **2012,** *5* (7), 7854-7863.
10. Mikhaylik, Y. V.; Akridge, J. R., Polysulfide Shuttle Study in the Li/S Battery System. *Journal of The Electrochemical Society* **2004,** *151* (11), A1969-A1976.
11. Mikhaylik, Y. V.; Kovalev, I.; Schock, R.; Kumaresan, K.; Xu, J.; Affinito, J., High Energy Rechargeable Li-S Cells for EV Application: Status, Remaining Problems and Solutions. *ECS Transactions* **2010,** *25* (35), 23-34.
12. Weng, W.; Pol, V. G.; Amine, K., Ultrasound Assisted Design of Sulfur/Carbon Cathodes with Partially Fluorinated Ether Electrolytes for Highly Efficient Li/S Batteries. *Advanced Materials* **2013,** *25* (11), 1608-1615.
13. Choi, J.-H.; Lee, C.-L.; Park, K.-S.; Jo, S.-M.; Lim, D.-S.; Kim, I.-D., Sulfur-impregnated MWCNT microball cathode for Li–S batteries. *RSC Advances* **2014,** *4* (31), 16062-16066.

14. Zheng, J.; Gu, M.; Wang, C.; Zuo, P.; Koech, P. K.; Zhang, J.-G.; Liu, J.; Xiao, J., Controlled Nucleation and Growth Process of Li2S2/Li2S in Lithium-Sulfur Batteries. *Journal of The Electrochemical Society* **2013,** *160* (11), A1992-A1996.
15. Cuisinier, M.; Cabelguen, P.-E.; Evers, S.; He, G.; Kolbeck, M.; Garsuch, A.; Bolin, T.; Balasubramanian, M.; Nazar, L. F., Sulfur Speciation in Li–S Batteries Determined by Operando X-ray Absorption Spectroscopy. *The Journal of Physical Chemistry Letters* **2013,** *4* (19), 3227-3232.
16. Scheers, J.; Fantini, S.; Johansson, P., A review of electrolytes for lithium–sulphur batteries. *Journal of Power Sources* **2014,** *255*, 204-218.
17. Camacho-Forero, L. E.; Smith, T. W.; Bertolini, S.; Balbuena, P. B., Reactivity at the lithium–metal anode surface of lithium–sulfur batteries. *The Journal of Physical Chemistry C* **2015,** *119* (48), 26828-26839.
18. Adams, B. D.; Black, R.; Williams, Z.; Fernandes, R.; Cuisinier, M.; Berg, E. J.; Novak, P.; Murphy, G. K.; Nazar, L. F., Towards a Stable Organic Electrolyte for the Lithium Oxygen Battery. *Advanced Energy Materials* **2015,** *5* (1).
19. Peng, H. J.; Huang, J. Q.; Cheng, X. B.; Zhang, Q., Lithium-Sulfur Batteries: Review on High-Loading and High-Energy Lithium–Sulfur Batteries (Adv. Energy Mater. 24/2017). *Advanced Energy Materials* **2017,** *7* (24), 1770141.
20. Park, M. S.; Ma, S. B.; Lee, D. J.; Im, D.; Doo, S.-G.; Yamamoto, O., A Highly Reversible Lithium Metal Anode. *Scientific Reports* **2014,** *4*, 3815.
21. Zhang, K.; Lee, G. H.; Park, M.; Li, W.; Kang, Y. M., Recent developments of the lithium metal anode for rechargeable non-aqueous batteries. *Advanced Energy Materials* **2016,** *6* (20), 1600811.
22. Aurbach, D.; Pollak, E.; Elazari, R.; Salitra, G.; Kelley, C. S.; Affinito, J., On the Surface Chemical Aspects of Very High Energy Density, Rechargeable Li–Sulfur Batteries. *Journal of The Electrochemical Society* **2009,** *156* (8), A694-A702.
23. Xu, W.; Wang, J.; Ding, F.; Chen, X.; Nasybulin, E.; Zhang, Y.; Zhang, J.-G., Lithium metal anodes for rechargeable batteries. *Energy & Environmental Science* **2014,** *7* (2), 513-537.
24. Lisbona, D.; Snee, T., A review of hazards associated with primary lithium and lithium-ion batteries. *Process Safety and Environmental Protection* **2011,** *89* (6), 434-442.
25. Peled, E., The Electrochemical Behavior of Alkali and Alkaline Earth Metals in Nonaqueous Battery Systems—The Solid Electrolyte Interphase Model. *Journal of The Electrochemical Society* **1979,** *126* (12), 2047.
26. Gabano, J.-P., *Lithium batteries*. 1983.
27. Matsuda, Y., Behavior of lithium/electrolyte interface in organic solutions. *Journal of Power Sources* **1993,** *43* (1), 1-7.
28. Aurbach, D.; Zinigrad, E.; Cohen, Y.; Teller, H., A short review of failure mechanisms of lithium metal and lithiated graphite anodes in liquid electrolyte solutions. *Solid State Ionics* **2002,** *148* (3), 405-416.
29. Huang, C.; Xiao, J.; Shao, Y.; Zheng, J.; Bennett, W. D.; Lu, D.; Saraf, L. V.; Engelhard, M.; Ji, L.; Zhang, J.; Li, X.; Graff, G. L.; Liu, J., Manipulating surface reactions in lithium–sulphur batteries using hybrid anode structures. *Nature Communications* **2014,** *5* (1), 3015.
30. Xu, K., Nonaqueous Liquid Electrolytes for Lithium-Based Rechargeable Batteries. *Chemical Reviews* **2004,** *104* (10), 4303-4418.
31. Balbuena, P. B.; Wang, Y., *Lithium-ion batteries: solid-electrolyte interphase*. Imperial college press: 2004.
32. Nie, M.; Abraham, D. P.; Chen, Y.; Bose, A.; Lucht, B. L., Silicon Solid Electrolyte Interphase (SEI) of Lithium Ion Battery Characterized by Microscopy and Spectroscopy. *The Journal of Physical Chemistry C* **2013,** *117* (26), 13403-13412.

33. Goriparti, S.; Miele, E.; De Angelis, F.; Di Fabrizio, E.; Proietti Zaccaria, R.; Capiglia, C., Review on recent progress of nanostructured anode materials for Li-ion batteries. *Journal of Power Sources* **2014,** *257*, 421-443.
34. Peled, E.; Golodnitsky, D.; Ardel, G., Advanced model for solid electrolyte interphase electrodes in liquid and polymer electrolytes. *Journal of the Electrochemical Society* **1997,** *144* (8), L208-L210.
35. Peled, E.; Menkin, S., Review—SEI: Past, Present and Future. *Journal of The Electrochemical Society* **2017,** *164* (7), A1703-A1719.
36. Martinez de la Hoz, J. M.; Soto, F. A.; Balbuena, P. B., Effect of the Electrolyte Composition on SEI Reactions at Si Anodes of Li-Ion Batteries. *The Journal of Physical Chemistry C* **2015,** *119* (13), 7060-7068.
37. Zhang, W.-J., A review of the electrochemical performance of alloy anodes for lithium-ion batteries. *Journal of Power Sources* **2011,** *196* (1), 13-24.
38. Etacheri, V.; Haik, O.; Goffer, Y.; Roberts, G. A.; Stefan, I. C.; Fasching, R.; Aurbach, D., Effect of Fluoroethylene Carbonate (FEC) on the Performance and Surface Chemistry of Si-Nanowire Li-Ion Battery Anodes. *Langmuir* **2012,** *28* (1), 965-976.
39. Verma, P.; Maire, P.; Novák, P., A review of the features and analyses of the solid electrolyte interphase in Li-ion batteries. *Electrochimica Acta* **2010,** *55* (22), 6332-6341.
40. Martinez de la Hoz, J. M.; Leung, K.; Balbuena, P. B., Reduction Mechanisms of Ethylene Carbonate on Si Anodes of Lithium-Ion Batteries: Effects of Degree of Lithiation and Nature of Exposed Surface. *ACS Applied Materials & Interfaces* **2013,** *5* (24), 13457-13465.
41. Ganesh, P.; Kent, P. R. C.; Jiang, D.-e., Solid–Electrolyte Interphase Formation and Electrolyte Reduction at Li-Ion Battery Graphite Anodes: Insights from First-Principles Molecular Dynamics. *The Journal of Physical Chemistry C* **2012,** *116* (46), 24476-24481.
42. Aurbach, D.; Ein-Ely, Y.; Zaban, A., The Surface Chemistry of Lithium Electrodes in Alkyl Carbonate Solutions. *Journal of The Electrochemical Society* **1994,** *141* (1), L1-L3.
43. Ma, Y.; Martinez de la Hoz, J. M.; Angarita, I.; Berrio-Sanchez, J. M.; Benitez, L.; Seminario, J. M.; Son, S.-B.; Lee, S.-H.; George, S. M.; Ban, C.; Balbuena, P. B., Structure and Reactivity of Alucone-Coated Films on Si and LixSiy Surfaces. *ACS Applied Materials & Interfaces* **2015,** *7* (22), 11948-11955.
44. Bertolini, S.; Balbuena, P. B., Buildup of the Solid Electrolyte Interphase on Lithium-Metal Anodes: Reactive Molecular Dynamics Study. *The Journal of Physical Chemistry C* **2018,** *122* (20), 10783-10791.
45. Sensato, F. c. R.; Custódio, R.; Calatayud, M.; Beltrán, A.; Andrés, J.; Sambrano, J. R.; Longo, E., Periodic study on the structural and electronic properties of bulk, oxidized and reduced SnO2(110) surfaces and the interaction with O2. *Surface Science* **2002,** *511* (1), 408-420.
46. Hong, N. H.; Sakai, J.; Poirot, N.; Brizé, V., Room-temperature ferromagnetism observed in undoped semiconducting and insulating oxide thin films. *Physical Review B* **2006,** *73* (13), 132404.
47. Beltrán, A.; Andrés, J.; Sambrano, J. R.; Longo, E., Density Functional Theory Study on the Structural and Electronic Properties of Low Index Rutile Surfaces for TiO2/SnO2/TiO2 and SnO2/TiO2/SnO2 Composite Systems. *The Journal of Physical Chemistry A* **2008,** *112* (38), 8943-8952.
48. Hassan, A.; Irfan, M.; Jiang, Y., Quantum confinement effect and size-dependent photoluminescence in laser ablated ultra-thin GZO films. *Materials Letters* **2018,** *210*, 358-362.
49. Bertolini, S.; Balbuena, P. B., Effect of solid electrolyte interphase on the reactivity of polysulfide over lithium-metal anode. *Electrochimica Acta* **2017,** *258*, 1320-1328.
50. Soto, F. A.; Ma, Y.; Martinez-DeLaHoz, J. M.; Seminario, J. M.; Balbuena, P. B., Formation and Growth Mechanisms of Solid-Electrolyte Interphase Layers in Rechargeable Batteries *Chem. Mater.* **2015,** *27* (23), 7990-8000.
51. Yen, Y.-C.; Chao, S.-C.; Wu, H.-C.; Wu, N.-L., Study on Solid-Electrolyte-Interphase of Si and C-Coated Si Electrodes in Lithium Cells. *Journal of The Electrochemical Society* **2009,** *156* (2), A95-A102.

52. Kim, S.-P.; Duin, A. C. T. v.; Shenoy, V. B., Effect of electrolytes on the structure and evolution of the solid electrolyte interphase (SEI) in Li-ion batteries: A molecular dynamics study. *Journal of Power Sources* **2011,** *196* (20), 8590-8597.
53. Jorn, R.; Kumar, R.; Abraham, D. P.; Voth, G. A., Atomistic Modeling of the Electrode–Electrolyte Interface in Li-Ion Energy Storage Systems: Electrolyte Structuring. *The Journal of Physical Chemistry C* **2013,** *117* (8), 3747-3761.
54. Philippe, B.; Dedryvère, R.; Allouche, J.; Lindgren, F.; Gorgoi, M.; Rensmo, H.; Gonbeau, D.; Edström, K., Nanosilicon Electrodes for Lithium-Ion Batteries: Interfacial Mechanisms Studied by Hard and Soft X-ray Photoelectron Spectroscopy. *Chemistry of Materials* **2012,** *24* (6), 1107-1115.
55. Schroder, K. W.; Celio, H.; Webb, L. J.; Stevenson, K. J., Examining Solid Electrolyte Interphase Formation on Crystalline Silicon Electrodes: Influence of Electrochemical Preparation and Ambient Exposure Conditions. *The Journal of Physical Chemistry C* **2012,** *116* (37), 19737-19747.
56. Philippe, B.; Dedryvère, R.; Gorgoi, M.; Rensmo, H.; Gonbeau, D.; Edström, K., Role of the LiPF6 Salt for the Long-Term Stability of Silicon Electrodes in Li-Ion Batteries – A Photoelectron Spectroscopy Study. *Chemistry of Materials* **2013,** *25* (3), 394-404.
57. Nguyen, C. C.; Lucht, B. L., Comparative Study of Fluoroethylene Carbonate and Vinylene Carbonate for Silicon Anodes in Lithium Ion Batteries. *Journal of The Electrochemical Society* **2014,** *161* (12), A1933-A1938.
58. Menkin, S.; Golodnitsky, D.; Peled, E., Artificial solid-electrolyte interphase (SEI) for improved cycleability and safety of lithium–ion cells for EV applications. *Electrochemistry Communications* **2009,** *11* (9), 1789-1791.
59. Liu, Y.; Lin, D.; Yuen, P. Y.; Liu, K.; Xie, J.; Dauskardt, R. H.; Cui, Y., An Artificial Solid Electrolyte Interphase with High Li-Ion Conductivity, Mechanical Strength, and Flexibility for Stable Lithium Metal Anodes. *Advanced Materials* **2017,** *29* (10), 1605531.
60. Wang, Y.; Nakamura, S.; Ue, M.; Balbuena, P. B., Theoretical Studies To Understand Surface Chemistry on Carbon Anodes for Lithium-Ion Batteries: Reduction Mechanisms of Ethylene Carbonate. *Journal of the American Chemical Society* **2001,** *123* (47), 11708-11718.
61. Leung, K.; Budzien, J. L., Ab initio molecular dynamics simulations of the initial stages of solid–electrolyte interphase formation on lithium ion battery graphitic anodes. *Physical Chemistry Chemical Physics* **2010,** *12* (25), 6583-6586.
62. Yu, J.; Balbuena, P. B.; Budzien, J.; Leung, K., Hybrid DFT Functional-Based Static and Molecular Dynamics Studies of Excess Electron in Liquid Ethylene Carbonate. *Journal of The Electrochemical Society* **2011,** *158* (4), A400-A410.
63. Agostini, M.; Scrosati, B.; Hassoun, J., An Advanced Lithium-Ion Sulfur Battery for High Energy Storage. *Advanced Energy Materials* **2015,** *5* (16), 1500481.
64. Camacho-Forero, L. E.; Balbuena, P. B., Elucidating electrolyte decomposition under electron-rich environments at the lithium-metal anode. *Phys. Chem. Chem. Phys.* **2017,** *19* (45), 30861-30873.
65. Kawaguchi, T.; Shimada, K.; Ichitsubo, T.; Yagi, S.; Matsubara, E., Surface-layer formation by reductive decomposition of LiPF6 at relatively high potentials on negative electrodes in lithium ion batteries and its suppression. *Journal of Power Sources* **2014,** *271*, 431-436.
66. Golodnitsky, D.; Livshits, E.; Ulus, A.; Peled, E., Highly conductive, oriented polymer electrolytes for lithium batteries. *Polymers for Advanced Technologies* **2002,** *13* (10-12), 683-689.
67. Perera, K. S.; Dissanayake, M. A. K. L.; Skaarup, S.; West, K., Application of polyacrylonitrile-based polymer electrolytes in rechargeable lithium batteries. *Journal of Solid State Electrochemistry* **2008,** *12* (7), 873-877.
68. Elia, G. A.; Park, J. B.; Sun, Y. K.; Scrosati, B.; Hassoun, J., Role of the Lithium Salt in the Performance of Lithium–Oxygen Batteries: A Comparative Study. *ChemElectroChem* **2014,** *1* (1), 47-50.

69. Plimpton, S., Fast Parallel Algorithms for Short-Range Molecular Dynamics. *Journal of Computational Physics* **1995,** *117* (1), 1-19.
70. Bedrov, D.; Smith, G. D.; van Duin, A. C. T., Reactions of Singly-Reduced Ethylene Carbonate in Lithium Battery Electrolytes: A Molecular Dynamics Simulation Study Using the ReaxFF. *The Journal of Physical Chemistry A* **2012,** *116* (11), 2978-2985.
71. Islam, M. M.; Bryantsev, V. S.; van Duin, A. C. T., ReaxFF Reactive Force Field Simulations on the Influence of Teflon on Electrolyte Decomposition during Li/SWCNT Anode Discharge in Lithium-Sulfur Batteries. *Journal of The Electrochemical Society* **2014,** *161* (8), E3009-E3014.
72. Chenoweth, K.; van Duin, A. C. T.; Goddard, W. A., ReaxFF Reactive Force Field for Molecular Dynamics Simulations of Hydrocarbon Oxidation. *The Journal of Physical Chemistry A* **2008,** *112* (5), 1040-1053.
73. Girifalco, L. A.; Weizer, V. G., Application of the Morse Potential Function to Cubic Metals. *Physical Review* **1959,** *114* (3), 687-690.
74. Mortier, W. J.; Ghosh, S. K.; Shankar, S., Electronegativity-equalization method for the calculation of atomic charges in molecules. *Journal of the American Chemical Society* **1986,** *108* (15), 4315-4320.
75. Tersoff, J., Empirical Interatomic Potential for Carbon, with Applications to Amorphous Carbon. *Physical Review Letters* **1988,** *61* (25), 2879-2882.
76. Brenner, D. W., Empirical potential for hydrocarbons for use in simulating the chemical vapor deposition of diamond films. *Physical Review B* **1990,** *42* (15), 9458-9471.
77. Aktulga, H. M.; Fogarty, J. C.; Pandit, S. A.; Grama, A. Y., Parallel reactive molecular dynamics: Numerical methods and algorithmic techniques. *Parallel Computing* **2012,** *38* (4), 245-259.
78. Rappe, A. K.; Goddard, W. A., Charge equilibration for molecular dynamics simulations. *The Journal of Physical Chemistry* **1991,** *95* (8), 3358-3363.
79. Yun, K.-S.; Pai, S. J.; Yeo, B. C.; Lee, K.-R.; Kim, S.-J.; Han, S. S., Simulation Protocol for Prediction of a Solid-Electrolyte Interphase on the Silicon-based Anodes of a Lithium-Ion Battery: ReaxFF Reactive Force Field. *The Journal of Physical Chemistry Letters* **2017,** *8* (13), 2812-2818.
80. Doll, K.; Harrison, N. M.; Saunders, V. R., A density functional study of lithium bulk and surfaces. *Journal of Physics: Condensed Matter* **1999,** *11* (26), 5007-5019.
81. Magda, J. J.; Tirrell, M.; Davis, H. T., Molecular dynamics of narrow, liquid-filled pores. *The Journal of Chemical Physics* **1985,** *83* (4), 1888-1901.
82. NosÉ, S., A molecular dynamics method for simulations in the canonical ensemble. *Molecular Physics* **2002,** *100* (1), 191-198.
83. Frisch, M. J.; Trucks, G. W.; Schlegel, H. B.; Scuseria, G. E.; Robb, M. A.; Cheeseman, J. R.; Scalmani, G.; Barone, V.; Petersson, G. A.; Nakatsuji, H.; Li, X.; Caricato, M.; Marenich, A. V.; Bloino, J.; Janesko, B. G.; Gomperts, R.; Mennucci, B.; Hratchian, H. P.; Ortiz, J. V.; Izmaylov, A. F.; Sonnenberg, J. L.; Williams; Ding, F.; Lipparini, F.; Egidi, F.; Goings, J.; Peng, B.; Petrone, A.; Henderson, T.; Ranasinghe, D.; Zakrzewski, V. G.; Gao, J.; Rega, N.; Zheng, G.; Liang, W.; Hada, M.; Ehara, M.; Toyota, K.; Fukuda, R.; Hasegawa, J.; Ishida, M.; Nakajima, T.; Honda, Y.; Kitao, O.; Nakai, H.; Vreven, T.; Throssell, K.; Montgomery Jr., J. A.; Peralta, J. E.; Ogliaro, F.; Bearpark, M. J.; Heyd, J. J.; Brothers, E. N.; Kudin, K. N.; Staroverov, V. N.; Keith, T. A.; Kobayashi, R.; Normand, J.; Raghavachari, K.; Rendell, A. P.; Burant, J. C.; Iyengar, S. S.; Tomasi, J.; Cossi, M.; Millam, J. M.; Klene, M.; Adamo, C.; Cammi, R.; Ochterski, J. W.; Martin, R. L.; Morokuma, K.; Farkas, O.; Foresman, J. B.; Fox, D. J. *Gaussian 16 Rev. C.01*, Wallingford, CT, 2016.
84. Roy Dennington, T. A. K., and John M. Millam *GaussView*, 6.1; Semichem Inc.: Shawnee Mission, KS, 2016.
85. Boese, A. D.; Martin, J. M. L., Development of density functionals for thermochemical kinetics. **2004,** *121* (8), 3405-3416.

86. Kendall, R. A.; Jr., T. H. D.; Harrison, R. J., Electron affinities of the first-row atoms revisited. Systematic basis sets and wave functions. **1992,** *96* (9), 6796-6806.
87. Han, J.; Balbuena, P. B., First-principles calculations of oxidation potentials of electrolytes in lithium-sulfur batteries and their variations with changes in environment. *Phys. Chem. Chem. Phys.* **2018,** *20* (27), 18811-18827.
88. Marenich, A. V.; Cramer, C. J.; Truhlar, D. G., Universal Solvation Model Based on Solute Electron Density and on a Continuum Model of the Solvent Defined by the Bulk Dielectric Constant and Atomic Surface Tensions. *The Journal of Physical Chemistry B* **2009,** *113* (18), 6378-6396.
89. Lin, F.; Markus, I. M.; Doeff, M. M.; Xin, H. L., Chemical and Structural Stability of Lithium-Ion Battery Electrode Materials under Electron Beam. *Scientific Reports* **2014,** *4* (1), 5694.
90. Egerton, R. F.; Li, P.; Malac, M., Radiation damage in the TEM and SEM. *Micron* **2004,** *35* (6), 399-409.
91. Sutton, L. E., *Tables of Interatomic Distances and Configuration in Molecules and Ions: Supplement 1956-59*. Chemical Society: 1965.
92. Abramowitz, S.; Acquista, N.; Levin, I. W., Infrared Matrix Spectra of Lithium Fluoride. *J Res Natl Bur Stand A Phys Chem* **1968,** *72A* (5), 487-493.
93. Martin, F.; Zipse, H., Charge distribution in the water molecule—A comparison of methods. *Journal of Computational Chemistry* **2005,** *26* (1), 97-105.
94. Assowe, O.; Politano, O.; Vignal, V.; Arnoux, P.; Diawara, B.; Verners, O.; van Duin, A. C. T., Reactive Molecular Dynamics of the Initial Oxidation Stages of Ni(111) in Pure Water: Effect of an Applied Electric Field. *The Journal of Physical Chemistry A* **2012,** *116* (48), 11796-11805.
95. Islam, M. M.; Kolesov, G.; Verstraelen, T.; Kaxiras, E.; van Duin, A. C. T., eReaxFF: A Pseudoclassical Treatment of Explicit Electrons within Reactive Force Field Simulations. *Journal of Chemical Theory and Computation* **2016,** *12* (8), 3463-3472.
96. Islam, M. M.; van Duin, A. C. T., Reductive Decomposition Reactions of Ethylene Carbonate by Explicit Electron Transfer from Lithium: An eReaxFF Molecular Dynamics Study. *The Journal of Physical Chemistry C* **2016,** *120* (48), 27128-27134.
97. Martinez de la Hoz, J. M.; Balbuena, P. B., Reduction mechanisms of additives on Si anodes of Li-ion batteries. *Physical chemistry chemical physics : PCCP* **2014,** *16* (32), 17091-8.
98. Cioslowski, J., A new population analysis based on atomic polar tensors. *Journal of the American Chemical Society* **1989,** *111* (22), 8333-8336.
99. Wang, A.; Kadam, S.; Li, H.; Shi, S.; Qi, Y., Review on modeling of the anode solid electrolyte interphase (SEI) for lithium-ion batteries. *npj Computational Materials* **2018,** *4* (1), 15.
100. Butler, K. T.; Sai Gautam, G.; Canepa, P., Designing interfaces in energy materials applications with first-principles calculations. *npj Computational Materials* **2019,** *5* (1), 19.
101. Shi, S.; Gao, J.; Liu, Y.; Zhao, Y.; Wu, Q.; Ju, W.; Ouyang, C.; Xiao, R., Multi-scale computation methods: Their applications in lithium-ion battery research and development. *Chinese Physics B* **2016,** *25* (1), 018212.
102. Kamphaus, E. P.; Hight, K.; Dermott, M.; Balbuena, P. B., Model systems for screening and investigation of lithium metal electrode chemistry and dendrite formation. *Phys. Chem. Chem. Phys.* **2020,** *22* (2), 575-588.
103. Li, Y.; Qi, Y., Energy landscape of the charge transfer reaction at the complex Li/SEI/electrolyte interface. *Energy Environ. Sci.* **2019,** *12* (4), 1286-1295.
104. Galvez-Aranda, D. E.; Ponce, V.; Seminario, J. M., Molecular dynamics simulations of the first charge of a Li-ion—Si-anode nanobattery. *Journal of Molecular Modeling* **2017,** *23* (4), 120.
105. Ponce, V.; Galvez-Aranda, D. E.; Seminario, J. M., Analysis of a Li-Ion Nanobattery with Graphite Anode Using Molecular Dynamics Simulations. *J. Phys. Chem. C* **2017,** *121* (23), 12959-12971.

106. Galvez-Aranda, D. E.; Seminario, J. M., Simulations of a LiF Solid Electrolyte Interphase Cracking on Silicon Anodes Using Molecular Dynamics. *Journal of The Electrochemical Society* **2018,** *165* (3), A717-A730.
107. Selis, L. A.; Seminario, J. M., Dendrite formation in silicon anodes of lithium-ion batteries. *RSC Adv.* **2018,** *8* (10), 5255-5267.
108. Galvez-Aranda, D.; Seminario, J. M., Ab Initio Study of the Interface of the Solid-State Electrolyte Li9N2Cl3 with a Li-Metal Electrode. *J. Electrochem. Soc.* **2019**, in press.
109. Longo, R. C.; Camacho-Forero, L. E.; Balbuena, P. B., Charge-mediated cation deposition on metallic surfaces. *Journal of Materials Chemistry A* **2019,** *7* (14), 8527-8539.
110. Camacho-Forero, L. E.; Balbuena, P. B., Exploring interfacial stability of solid-state electrolytes at the lithium-metal anode surface. *J. Power Sources* **2018,** *396*, 782-790.
111. Camacho-Forero, L. E.; Balbuena, P. B., Effects of charged interfaces on electrolyte decomposition at the lithium metal anode. *J. Power Sources* **2020,** *472*, 228449.
112. Leung, K.; Rempe, S. B.; Foster, M. E.; Ma, Y.; Martinez-delaHoz, J. M.; Sai, N.; Balbuena, P. B., Modeling Electrochemical Decomposition of Fluoroethylene Carbonate on Silicon Anode Surfaces in Lithium Ion Batteries. *J. Electrochem. Soc.* **2014,** *3*, A213-221.
113. Leung, K., Predicting the voltage dependence of interfacial electrochemical processes at lithium-intercalated graphite edge planes. *Physical chemistry chemical physics : PCCP* **2015,** *17*, 1637-1643.
114. Leung, K.; Leenheer, A., How Voltage Drops Are Manifested by Lithium Ion Configurations at Interfaces and in Thin Films on Battery Electrodes. *J. Phys. Chem. C* **2015,** *119* (19), 10234-10246.
115. Li, Y.; Li, Y.; Pei, A.; Yan, K.; Sun, Y.; Wu, C.-L.; Joubert, L.-M.; Chin, R.; Koh, A. L.; Yu, Y.; Perrino, J.; Butz, B.; Chu, S.; Cui, Y., Atomic structure of sensitive battery materials and interfaces revealed by cryo–electron microscopy. **2017,** *358* (6362), 506-510.
116. Huang, W.; Wang, H.; Boyle, D. T.; Li, Y.; Cui, Y., Resolving Nanoscopic and Mesoscopic Heterogeneity of Fluorinated Species in Battery Solid-Electrolyte Interphases by Cryogenic Electron Microscopy. *ACS Energy Letters* **2020,** *5* (4), 1128-1135.
117. Zachman, M. J.; Tu, Z.; Choudhury, S.; Archer, L. A.; Kourkoutis, L. F., Cryo-STEM mapping of solid–liquid interfaces and dendrites in lithium-metal batteries. *Nature* **2018,** *560* (7718), 345-349.
118. Jurng, S.; Brown, Z. L.; Kim, J.; Lucht, B. L., Effect of electrolyte on the nanostructure of the solid electrolyte interphase (SEI) and performance of lithium metal anodes. *Energy Environ. Sci.* **2018,** *11* (9), 2600-2608.
119. Li, X.; Zheng, J.; Ren, X.; Engelhard, M. H.; Zhao, W.; Li, Q.; Zhang, J.-G.; Xu, W., Dendrite-Free and Performance-Enhanced Lithium Metal Batteries through Optimizing Solvent Compositions and Adding Combinational Additives. **2018,** *8* (15), 1703022.
120. Wang, Z.; Qi, F.; Yin, L.; Shi, Y.; Sun, C.; An, B.; Cheng, H.-M.; Li, F., An Anion-Tuned Solid Electrolyte Interphase with Fast Ion Transfer Kinetics for Stable Lithium Anodes. **2020,** *10* (14), 1903843.
121. Park, S.-J.; Hwang, J.-Y.; Yoon, C. S.; Jung, H.-G.; Sun, Y.-K., Stabilization of Lithium-Metal Batteries Based on the in Situ Formation of a Stable Solid Electrolyte Interphase Layer. *ACS Appl. Mater. Interfaces* **2018,** *10* (21), 17985-17993.
122. Shi, S. Q.; Lu, P.; Liu, Z. Y.; Qi, Y.; Hector, L. G.; Li, H.; Harris, S. J., Direct Calculation of Li-Ion Transport in the Solid Electrolyte Interphase. *Journal of the American Chemical Society* **2012,** *134* (37), 15476-15487.

Table of Contents Graphic